TÉCNICO LISBOA

Wireless Power Transfer System
For Electric Vehicle Charging

Pedro Miguel Conceição Lopes

Thesis to obtain the Master of Science Degree in

Electrical and Computer Engineering

Supervisors: Prof. Sónia Maria Nunes dos Santos Paulo Ferreira Pinto

Mestre Pedro Miguel Batista de Sousa Correia da Costa

Examination Committee

Chairperson: Prof. Célia Maria Santos Cardoso de Jesus

Supervisor: Prof. Sónia Maria Nunes dos Santos Paulo Ferreira Pinto

Member of the Committee: Prof. Miguel Cabral Ferreira Chaves

January 2021

Declaration

I declare that this document is an original work of my authorship and that it fulfills all the requirements of the Code of conduct and Good Practices of the Universidade de Lisboa.

Acknowledgments

Firstly, I have to thank my supervisor, Prof. Sónia Pinto, for all the vital continuous support, availability, and counseling given to me since the beginning of my work and for believing from the start and also through the school year that this thesis would be finished in time with all the initial goals achieved.I also would like to thank the project of the FCT, PTDC/EEI-EEE/32550/2017-Smart Transformers for Sustainable Grids, for the inclusion of my thesis in their research.

Secondly, I have to thank my co-supervisor, Pedro Costa, which also provide me with an incredible amount of counseling and support during my work, especially during the experimental phase, for which I am very grateful and sure that if not provided the experimental results obtained would not have been possible.

I would also like to thank my family for all their unconditional support. Since the begging of my academic journey and life, they always have been present to listen to me and help me in any way possible, for which I will always be grateful.

To all my close friends, for being present every time I need to relax and have a good laught.

Finally, I would like to thank the Instituto Superior Técnico de Lisboa and all their member for all the excellent education and life values I received during this 5 years journey.

Resumo

A pesquisa sobre novas formas de carregar um veículo elétrico (VE) é um tema de pesquisa popular. Carregamento sem fios é uma das muitas tecnologias atualmente a ser investigadas e selecionadas para uma variedade de aplicações. Com esta tecnologia não existe nenhuma conexão física entre o VE e a estação de carregamento, proporcionando uma experiência agradável entre o veículo e o usuário.No entanto, levanta-se a questão sobre o quão bem esta se comporta em comparação com outras tecnologias de carregamento de VE.

Esta tese estuda o comportamento de um protótipo de um sistema de transferência de energia sem fios para VE's que foi projetado e construído para analisar e compreender o processo de carregamento sem fios.

Uma primeira análise foi feita sobre os princípios de operação da transferência de energia sem fios apoiada no estado da arte das tecnologias utilizadas atualmente. O carregamento ressonante sem fios foi selecionado como o melhor candidato para o modelo de protótipo com base nas demandas físicas e de energia. Foram mencionados conceitos importantes relacionados a essas tecnologias, como redes de compensação e comutação com tensão zero e corrente zero.

Um protótipo de carregador indutivo de 100 W usando um tanque ressonante foi projetado e testado usando o software Simulink e Matlab.Dimensionou-se e simulou-se um controlador para controlar a tensão de carga. Foi construído um protótipo à escala realizaram-se testes experimentais para validar a topologia proposta e o controlador. Os resultados obtidos foram analisados e as conclusões foram tiradas em relação ao desempenho geral do carregador indutivo ressonante.

Palavras-Chaves: Carregamento sem fios, Veículos Elétricos, Transferência de energia, Tanque ressonante, Carregador indutivo.

Abstract

The research regarding new ways of charging an electric vehicle (EV) is a treading research topic. Wireless charging is one of many technologies currently being investigated and preferred for various applications. With this technology, there is no physical connection between the EV and the charging station, providing a pleasant experience between the vehicle and the user. However, the question arises about how well it performs compared with other technologies of EV's.

This thesis studied the behavior of a prototype of a wireless power transfer system for EVs that was designed and built to analyze and understand the wireless charging process.

A first analysis was made on the operating principles of wireless power transfer supported on the state of the art of the currently used technologies. The resonant wireless charging was selected as the best candidate for the prototype model based on physical and power demands. Important concepts related to these technologies were mentioned, such as zero voltage and zero current switching and compensation networks.

A 100 W inductive charger prototype using a resonant tank was designed and tested using the Simulink and Matlab software. A controller was dimensioned and simulated to control the load voltage. A prototype was built to scale, and experimental tests were carried out to validate the proposed topology and controller. The experiment data was analyzed, and conclusions were drawn regarding the resonant inductive charger's overall performance.

Keywords: Wireless Charging, Electrical Vehicles, Power Transfer, Resonant tank, Inductive charger

Contents

List of figures

List of tables

Variables

$\dot{I}$	Complex current
$\dot{S}$	Complex apparent power
$\dot{U}$	Complex voltage
C_{iss}	Input Capacitance
C_{rss}	Reverse Transfer Capacitance
C_g	Gate Capacitance
f_r	Resonant linear frequency
f_{sw}	Switching frequency
I	Phase current amplitude
I_{Smax}	Maximum current across transistor S
I_{Srms}	Root Mean Square current across transistor S
k	Coupling coefficient
K_i	Integral gain
K_p	Proportional gain
L	Inductance
M	Mutual inductance
P_{CON}	Conduction power losses
P_d	Total power losses
P_{sw}	Switching power losses
Q_g	Gate Charge
Q_L	Resonant factor
R	Resistance
r	Turn ratio
R_D	Diode forward resistance
R_{DSon}	Drain to Source On resistance
R_g	Gate Resistance
S	Phase apparent power
T_d	Statistical delay
T_p	Pole of the controller
T_z	Zero of the controllers

T_{sw}	Switching period
t_f	Fall time
t_r	Rise time
U	Phase voltage amplitude
V	Effective voltage
V_{dd}	Instantaneous voltage across the transistor
α	Voltage gain
δ	Phase angle
Δi_0	Ripple Current
ξ	Damping coefficient
φ	Phase difference
θ	Shift angle
ω	Angular frequency
ω_0	Resonant angular frequency
ω_s	Switching angular frequency
ω_n	Natural angular frequency

Acronyms

AC	Alternating Current
ADC	Analog to Digital Converter
BEV	Battery Electrical Vehicle
CCM	Continuous-Conduction Mode
CWPT	Capacitive Wireless Power Transfer
DC	Direct Current
DCM	Discontinuous-Conduction Mode
EMI	Electromagnetic Interference
EV	Electric Vehicle
FOM	Figure of Merit
HEV	Hybrid Electrical Vehicle
IPT	Inductive Power Transfer
IGBT	Insulated gate bipolar transistor
MOSFET	Metal Oxide Semiconductor Field Effect Transistor
NHV	Noise, Vibration, and Harshness
NPP	Non-Polarized Pads
PCB	Printed Circuit Boards
PLR	Parallel-Loaded Resonant
PM	Permanent Magnets
PMCPT	Permanent Magnets Coupling Power Transfer
PP	Polarized Pads
PWM	Pulse Width Modulation
RIPT	Resonant Inductive Power Transfer
SMD	Surface-Mounted Devices
SLR	Series-Loaded Resonant
VSC	Voltage Source Converter
WCS	Wireless Charging Systems
WEVCS	Wireless Electric Vehicle Charging Systems
WPT	Wireless Power Transfer
WPTS	Wireless Power Transfer Systems

ZCS	Zero Current Switching
ZVS	Zero Voltage Switching

1. Introduction

The need for sustainable means of transportation, caused by the depletion of fossil fuels, has led to the growth in Electric Vehicle (EV) technologies' research and innovation. According to 2020 Global EV Outlook [1], an annual publication that identifies and discusses recent electric mobility developments worldwide, EVs' sales continue to rise. In 2019, 2.1 million were sold, surpassing 2018, registering a 40% year-on-year increase, which leads to the assumption that EV's are a solution to continue to grow over the following years. A global EV forecast [2] predicts a total EV sales growing from 2.5 million in 2020 to 11.2 million in 2025, then reaching 31.1 million by 2030.

Carbon emissions raise severe challenges for the sustainability of future generations. Part of this risk is due to the transportation industry [3]. According to the Health World Organization, transportation accounted for about 23% of global carbon dioxide emissions in 2010 and 27% of end-use energy emissions, with urban transport accounting for about 40% of end-use energy consumption [4].

One solution to lower the carbon dioxide emissions caused by the urban transportation sector is to replace fossil-based fuels with green sources such as electrical energy [5]. Vehicles that use electrical energy as their primary source of power are the so-called electrical vehicles. An EV can be categorized broadly into Battery electric vehicle (BEV), which runs solely on electricity and the hybrid electric vehicle (HEV) that combines the electric energy with other sources of renewable energy or in many cases they have a standard internal combustion engine that runs in fossil-fuel [6]. Nowadays, these vehicles mainly use Li-Ion batteries [7]. Most of the current EV chargers are cable-based. However, wireless power transfer (WPT) solutions are becoming more attractive as the power and conversion efficiency has increased in the last few years. The global wireless electric vehicle charging market was valued at 7.6 million dollars in 2019, with expectations to reach 210 million dollars by 2030 [8].

Wireless charging consists of transferring energy from the source to the load without the need for any wires. WPT is not new, as Nikola Tesla had patented WPT over 100 years ago [9]. Nowadays, WPT systems are used both on short and long-range applications. There are some examples of electric toothbrushes on short-range applications that use inductive charging and, more recently, smartphone chargers. The WPT systems used on EV's are considered long-range applications.

Besides this classification of long and short-range, wireless charging systems (WCS) can be used in a static mode where the battery is charged when the vehicle is parked, or in a dynamic model where the battery is being charged when the EV is in motion [10]. This thesis focused on stationary WCS.

The large majority of the WPT systems are inductive power transfer (IPT) systems. According to [11], IPT systems are defined as systems where energy is transferred from a primary winding to a secondary using a magnetic field. Such systems can be divided into two categories: 1) closely coupled IPT systems

and 2) loosely coupled IPT systems. In closely coupled IPT systems, the magnetic coupling between the primary and the secondary side is perfect, i.e., the leakage inductance is small compared to the magnetizing inductance in the system. The second system is the opposite: the magnetic coupling between both sides is low, and the leakage inductance is usually much higher than the magnetizing inductance of the system, resulting in low efficiency of the charging process.

The main goal of all the research being done on this topic is to study the wireless charging process and draw conclusions based on experiments performed in a real designed prototype.

1.1. Objectives

The following objectives are defined for this work:

- Review on the background and state-of-art of WPTS;
- Establish the link between the thesis topic and the state-of-art;
- Design of a loosely coupled IPT system based on current WPT technologies to optimize the general efficiency of the process;
- To design a simulation model of an inductive charger;
- Design a control system to command the semiconductors;
- Design and build an experimental prototype to validate both the designed controller and the selected topology;
- Provide results and documentation for the future development of this technology.

1.2. Thesis outline

In the first chapter, an introduction to the motivation and the objectives for this thesis is made. It is mentioned why having renewable energy sources is essential and why they should be used for powering vehicles. It is explained the concept of a WPTS. And finally, a detailed list was elaborated, stating all objectives intended to be achieved by the end of the research.

The second chapter presents a brief review of the state-of-art of the WPTS and a generic explanation of how IPT systems work, including normalized models with mathematical formulations. The introduction is mentioning the main topologies currently used for WPT systems. Important topics were explained, like compensation networks and zero voltage and zero current switchings. And finally, it is presented a general overview of the advantages and disadvantages of all the topologies mentioned before and some examples of real WCS currently in the market or current development.

In the third chapter, to understand the working principle of WPTS better, a simulation of an inductive charger was performed. Each block of the simulation was explained, including how the control system controls the semiconductors.

The fourth chapter presents the simulation results, which are analyzed, documented, and considered when building the physical inductive charger.

The fifth chapter explains the building process of the PCB's. Two boards, one for the converter on the primary side and the other for the converter on the resonant tank's exit. A process of selecting each type and model of the semiconductor and substantial additional circuitry was mentioned, such as the gate drivers and the voltage and current sensors. Lastly, there are some pictures of the final PCB assembled as well of the prototype built ready to perform experiments

In chapter six, after performing the simulation and building the prototype, some experiments were made to study the charging process, and the results of the experiment were showed and analyzed.

Finally, in chapter seven, conclusions were drawn about the developed work regarding the objectives outlined at the beginning of the thesis and some future work suggestions.

2. Background and State-Of-Art

The standard block diagram of a WPT system used for an Electric Vehicle (EV) is illustrated in Figure 1 [10]. This early stage of the work let this generic block diagram represent an IPT system used in most WPTS. Even though the figure shows the power transferred by two coils, it is possible to use different energy transfer methods.

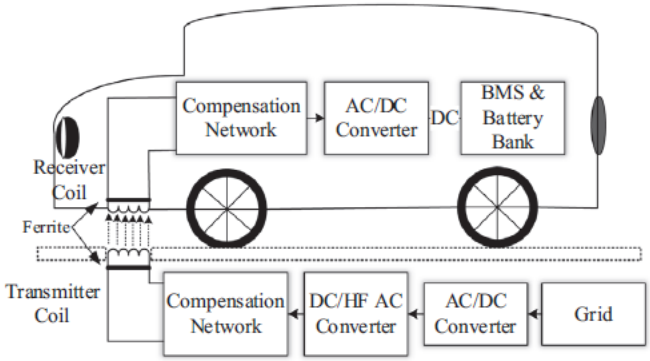

Figure 1-Basic block diagram of WPT (Courtesy of C.Panchal et al.).

In this specific typology, the grid's AC voltage is converted first to DC and then to high frequency (HF)AC voltage. The compensation network improves the overall efficiency of the charging process. This compensation network includes both the receiving and transmitting sides, which can have different configurations. On the vehicle side, the receiver coil delivers the transmitter coil's power to the on-board charger. This process comprises 3 essential parts:

- The transmitting and receiving coils. These coils may assume different shapes and types of materials that influence the charging process's overall efficiency, as is going to be shown in later sections.
- The compensation networks.
- The power electronics converters.

A simplification was made, where the power electronics converters, for now, are not considered, and the compensation networks are only shown as a white box where the power goes through.

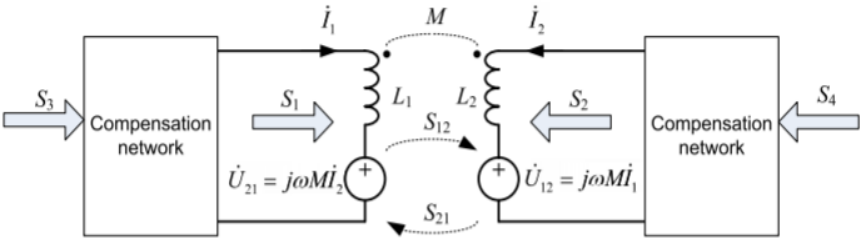

Figure 2-Two-coil WPT system (Courtesy of S.Li et al.).

By looking at Figure 2, it is possible to identify L_1 which is the self-inductance of the primary side or transmitting coil and L_2 represents the self-inductance of the secondary side or receiving coil. $\dot{I}_1$ and $\dot{I}_2$ are the currents in the two coils, $\dot{U}_{12}$ is the voltage in the secondary coil that is induced by the current in the primary side, $\dot{U}_{21}$ is the voltage in the primary coil induced by the secondary coil current due to coupling or mutual inductance between the primary and secondary coils. S_1 and S_2 are the apparent power provided by the power converter. $\dot{S}_{12}$ and $\dot{S}_{21}$represent the apparent power exchanged between the two coils. For this analysis, the coil resistance and magnetic losses are neglected and, from L_1 and L_2, it is possible to formulate the equations of the exchanged complex power: $\dot{S}_{12}$ (1) and $\dot{S}_{21}$ (2), where I_1 and I_2 are the root, mean square values of the currents and φ_{12} is the phase difference between $\dot{I}_1$ and $\dot{I}_2$.

$$\begin{aligned}\dot{S}_{12} &= -\dot{U}_{12}\dot{I}^{*}_{2} = -j\omega M\dot{I}_1\dot{I}^{*}_{2} = \\ &= \omega M I_1 I_2 \sin\varphi_{12} - j\omega M I_1 I_2 \cos\varphi_{12}\end{aligned} \tag{1}$$

$$\begin{aligned}\dot{S}_{21} &= -\dot{U}_{21}\dot{I}^{*}_{1} = -j\omega M\dot{I}_2\dot{I}^{*}_{1} = \\ &= -\omega M I_1 I_2 \sin\varphi_{12} - j\omega M I_1 I_2 \cos\varphi_{12}\end{aligned} \tag{2}$$

From (1), the active power transfer from the primary side to the secondary can be maximized by assuring that the phase difference between both current, φ_{12} , is around 90 º as expressed:

$$P_{12} = \omega M I_1 I_2 \sin\varphi_{12} \tag{3}$$

Assuming $\varphi_{12} = \frac{\pi}{2}$, means that the total complex power that goes into the two-coil system is then given by:

$$\begin{aligned}\dot{S} &= \dot{S}_1 + \dot{S}_2 = j(\omega L_1\dot{I}_1 + \omega M\dot{I}_2)\dot{I}^{*}_{1} - j(\omega L_2\dot{I}_2 + \omega M\dot{I}_1)\dot{I}^{*}_{2} = \\ &= j\omega(L_1 I_1^{\,2} + L_2 I_2^{\,2} + 2M I_2 I_1 \cos\varphi_{12})\end{aligned} \tag{4}$$

Therefore, the reactive power *Q* that goes into the two-coil system is:

$$Q = \omega(L_1 I_1^{\,2} + L_2 I_2^{\,2} + 2M I_2 I_1 \cos\varphi_{12}) \tag{5}$$

From the fundamentals of traditional transformers, reactive power represents the magnetizing power. Thus, higher magnetizing power results in higher copper and core losses. When computing the efficiency of transformers, two essential parameters come to play. One is the coupling coefficient of the windings or the quality of the magnetic circuit usually expressed by *k*, and the other is the quality factor Q_L. The coupling coefficient appears in the expression of the mutual inductance *M:*

$$M = k\sqrt{L_1 L_2} \tag{6}$$

The coupling coefficient *k* ranges from 0 to 1, where 1 means that all the magnetic flux produced from one coil passes through the other coupled coil, and so the efficiency becomes higher. The inductor quality factor Q_L is given by the ratio between the inductor reactance and its resistance at a given frequency:

$$Q_L = \frac{\omega_L}{R_L} \tag{7}$$

The quality factor Q_L is also related to the efficiency of the process since higher Q_L means the coil's behavior is closer to an ideal inductor. For stationary EV wireless charging, the coupling between the two coils is usually around 0.2.

2.1. Coil Systems Design

The shape, size, location of the magnetic core material and winding play a crucial role in the WPT efficiency. The typical coil systems are the two-coil structure shown in Figure 1 and the four-coil system [12], represented in Figure 3.

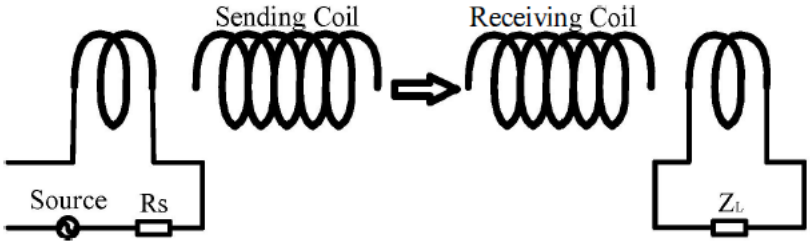

Figure 3-Four-Coil structure (Courtesy of Z.Liu et al.).

Compared to the two-coil system, the four-coil system offers the advantage of having two degrees of freedom where the source coil can be mounted and coupled with the sending coil to adjust the system input impedance, and the same logic can be used for the load coil that when coupled with the receiving coil, adjusts the equivalent load resistance. A four-coil system is suitable for mid-range applications, while a two-coil system performs better for short-range applications [12].

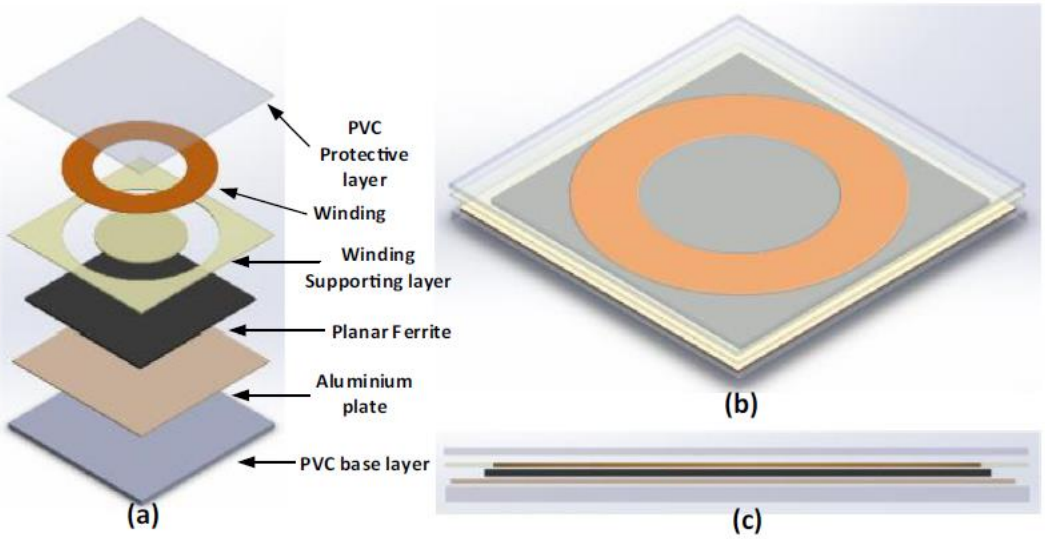

Figure 4-Wireless Transformer (a) exploded view (b) Top view (c) Cross-section (Courtesy of Z.Liu et al.).

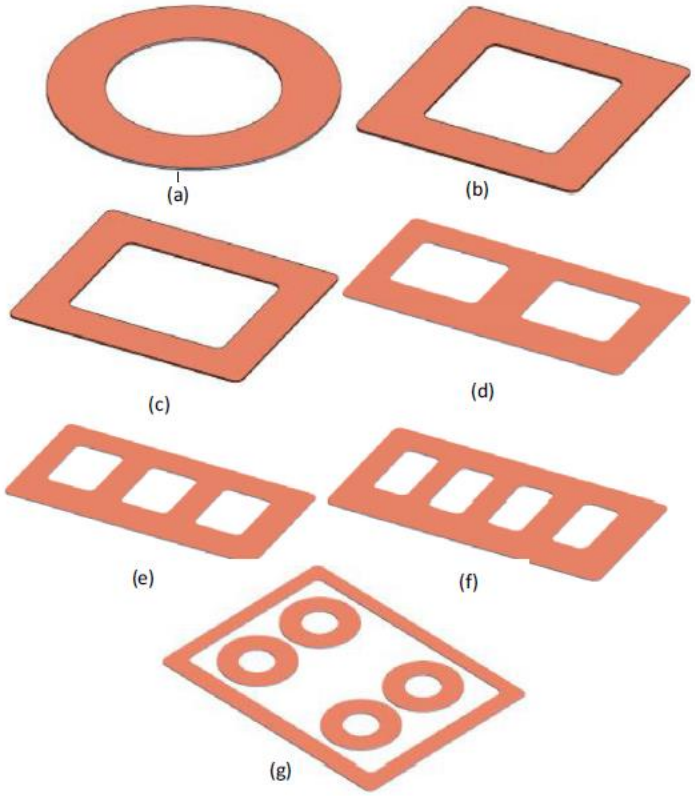

Figure 5-Coil shapes (a) Circular (b) Square (c) Rectangular (d) Double D (e) Bi-polar (Courtesy of Z.Liu et al.).

In EV applications, the transmission distance, or air gap, ranges from 100 mm to 300 mm [13]. Since the coil dimension is always bigger than the transmission distance, the two-coils system is preferred. Besides the coils, it is necessary to have a material to guide the magnetic flux and provide magnetic shielding. The typical material used for guiding the magnetic flux is ferrite bars or plates, and for the shielding, aluminum shields are often used. The shielding is essential to reduce the magnetic leakage from the magnetic flux produced by the coil system.

To guarantee maximum power transfer efficiency and lower EMI, the transmitter and receiver pads must be designed with multiple component layers, as shown Figure 4 [10]. The three highlighted components of the wireless transformer pads are the coils, shielding material (ferrite and aluminum plate), and the proactive and supporting layers.

As shown in Figure 5 [13], different coil shapes can be used for WPT applications. It is possible to use circular, rectangular, or even hybrid arrangements used to improve performance and solve misalignment problems.

Wireless coils are divided into polarized pads (PP) and Non-polarized pads (NPP). The PP is created from multiple coils and generate perpendicular and parallel components of flux, while the NPP is made from one single-coil shape and produce only perpendicular components of flux [14].

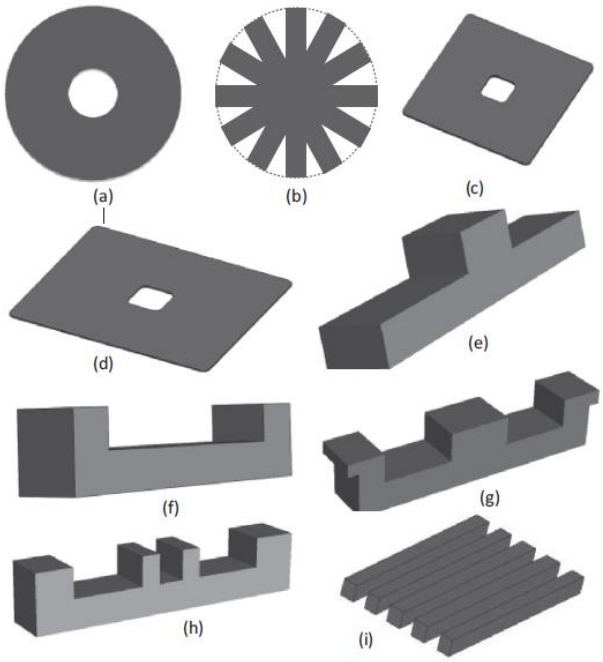

Figure 6-Ferrite shapes (a) Circular (b) circular striated (c) square (d) rectangular (e) T-core (f) U-core (G) E-core (h) Double U (i) striated blocks(Courtesy of Z.Liu et al).

The shapes of the magnetic ferrites also play an essential role in how efficient the power transfer process is since the ferrite will be responsible for the magnetic flux's conduction. The choice of ferrite shape

and material influences efficiency, but it is also a safety measure since magnetic leakage can negatively impact personal health [10] . The way the ferrite core is chosen depends on multiple factors such as size, shape permeability, operating frequency, and cost. Basic ferrite shapes are shown in Figure 6.

Aluminum plating is used in Wireless Electric Vehicle Charging Systems (WEVCS) to reduce the flux leakage and improve Wireless Charging Systems (WCS). Since, in most cases, the transmitter pad is mounted underneath the concrete structure of the road, this pad needs to handle the car's weight and additional vibration of the vehicle. Therefore, PVC plastic sheets are used in the bottom and top layers to improve structure stability [10].

2.2. Permanent Magnet Coupling Power Transfer (PMCPT)

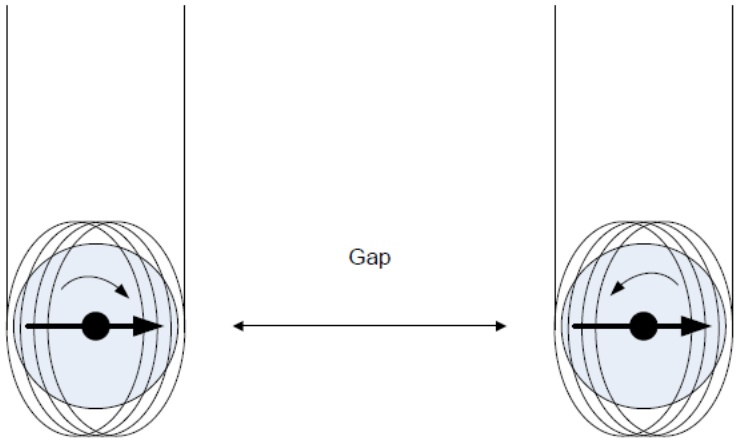

Figure 7-Co-rotating PM cores inside a two coil-system (Courtesy of L.Weilai et al).

As shown in Figure 7, this topology uses the coupling of two permanent magnets (PM). For this method to work, the PMs are positioned side-by-side and are synchronized with each other. The energy transferred from one magnet to the other is done by applying torque from the PM on the PM's primary side on the secondary. This produces mechanical energy that is transformed into electrical energy. When both PMs are synchronized, the primary PM works as a generator, and the secondary PM receives the power delivering to the power electronics that is responsible for supplying the battery of the EV.

An advantage of this method is that the inherent losses are very negligible. By rotating the primary PM at a constant speed, produces a time-varying magnetic field. Then this magnetic field is used to rotate the secondary PM. This rotation of two synchronized PMs consumes very little power, assuming no eddy currents or hysteresis losses. Compared to other WPT systems, this method operates with much lower frequencies, 2-3 orders of magnitude lower, not having the difficulties of high-frequency operation. [15].

It is possible to better understand the power transfer process between the transmitter and receiver sides by looking at Figure 8.

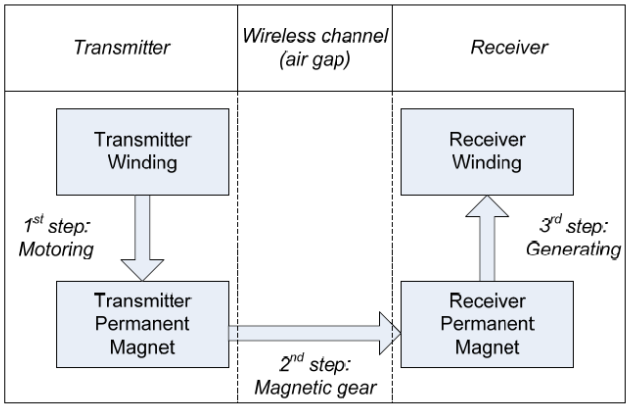

Figure 8-Power flow of the proposed method (Courtesy of L.Weilai et al.).

The following steps can describe this process:

1. An electric current is delivered to the transmitting winding. The current produces a mechanical torque on the Transmitter PM, initializing its rotation. This process is like the one of a motor because electrical energy is being transformed into mechanical energy.
2. By placing the receiver PM close enough to the transmitter PM, the primary PM produces a torque in the secondary PM, causing it to rotate synchronously with the transmitter PM. The power is transferred across the air gap, as shown in the figure.
3. The PM inside the receiving winding rotates, producing a time-varying magnetic flux creating an induced current. Then the mechanical power is converted to electrical power.

2.3. Capacitive Wireless Power Transfer (CWPT)

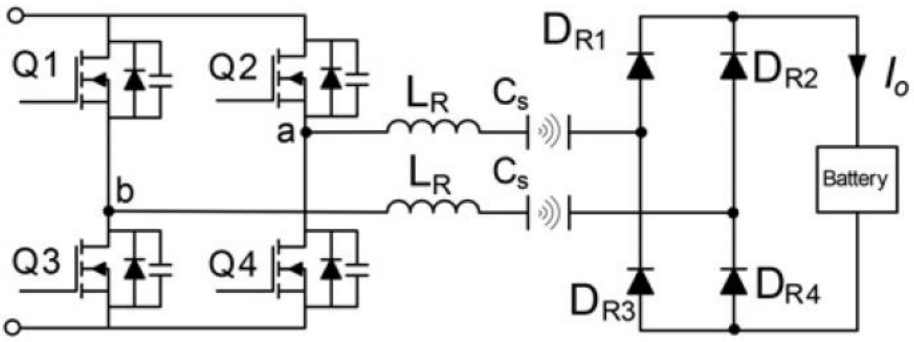

Figure 9-Diagram of CWPT (Courtesy of M. Fariborz et al.).

This topology uses geometric and mechanical structures of coupling capacitors. The CWPT systems use coupling capacitors to couple or link together both sides of the circuit. The DC component of the AC signal originated from the primary side is blocked thanks to this capacitor, passing only the signal's AC component. As shown in Figure 9, the remaining of the power conversion system remains the same as the conventional IPT system. This capacitive interface can bring down the cost and size of the galvanic isolation using this method [16]. However, this thesis aims to study WPT systems for high power applications, which is not the right solution since CWPT systems are used for lower power devices such as wireless cell phone chargers or wireless toothbrushes chargers.

2.4. Resonant Inductive Power Transfer (RIPT)

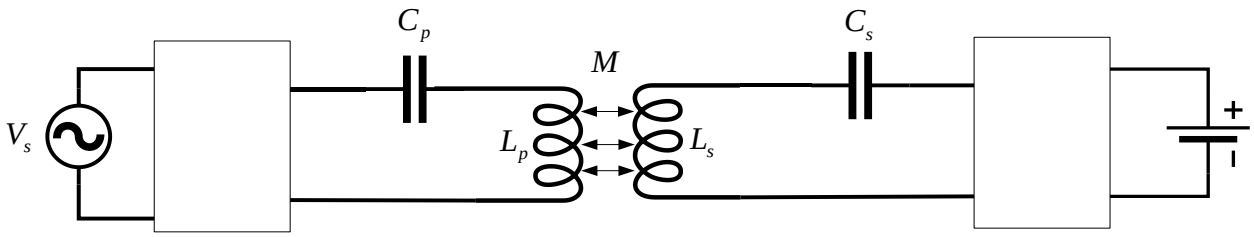

Figure 10-Resonant inductive charger.

RIPT is the most popular WPT technology [16]. This technique uses two or more tuned resonant tanks, based on LC circuits, resonating at the same frequency. A typical example is shown in Figure 10, where both sides of the charger have a capacitor and an inductance.

Using resonant circuits bring many advantages, such as:

- Maximizing the transferred power;
- Optimizing the transmission efficiency;
- Controlling the transmitted power by frequency variation;
- Creating a specific source characteristic (current or voltage source);
- Compensating variation of the magnetic coupling;
- Compensating the magnetizing current in the transmitter coil to reduce generator losses;
- Matching the transmitter coil impedance to the generator;
- Suppressing higher harmonics form the generator;

From the schematic diagram, it is possible to see how the power flows from the grid to the EV batteries. The primary AC voltage is converted into HF AC voltage being transferred to the secondary side. Then the power is converted to DC to supply the batteries, using a diode bridge rectifier.

The capacitors added to the system are usually called compensation capacitors. They are placed in series and/or parallel combinations on both sides to create the RIPT. Different types of combinations can influence the charging process.

On [16], the efficient resonant magnetic coupling can be achieved at distances up to 40 cm. Compared to the traditional IPT, RIPT has significant advantages, including the increased range, reduced EMI, higher frequency operation, resonant switching of the inverter and the receiver rectification circuitry, and higher efficiency. The main advantage of this method is that it is possible to operate with frequencies in the order of tens of kHz to MHz.

2.5. Compensation Networks

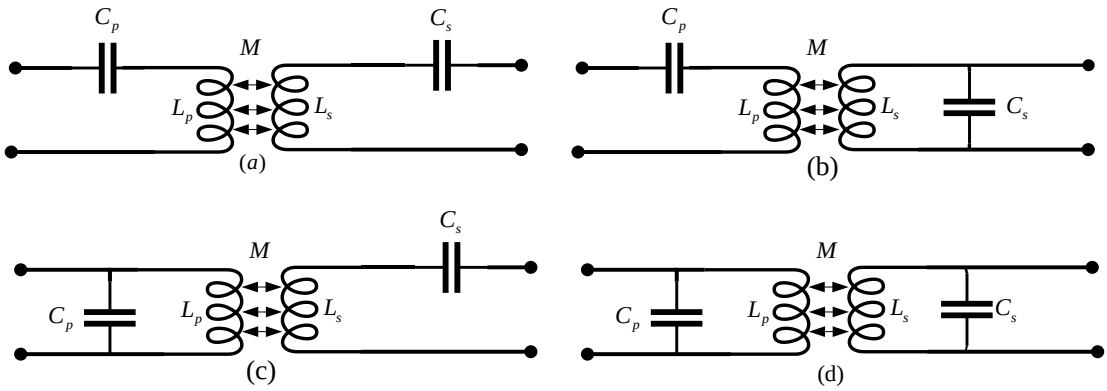

Figure 11-Compensation Topology (a) Series-Series (b) Series-Parallel (c) Parallel-Series (d) Parallel-Parallel.

As shown in Figure 11 [13], capacitors introduction on the primary and secondary sides are essential to eliminate the phase difference between current and voltage and minimize the reactive power in the power source. The compensation network is also responsible for tuning the circuit to have the same resonance frequency as the transmitter to maximize the power transfer. Other benefits of using compensation networks are the help they give to have a soft switching of power transistors, reduce switching losses, and have constant current and constant voltage charging [13]. It is fair then to assume that even though having more elements implies having a more complex topology. It is essential to have a compensation network when designing a WPTS since it benefits the charging process. The four main types of compensation network topologies are shown in Figure 11 :

- Series-Series (SS)
- Series-Parallel (SP)
- Parallel-Series (PS)
- Parallel-Parallel (PP)

The PS and PP topologies protect the WCS if the source coil does not operate in the absence of the receiving coil. The misalignment is a significant factor in power transfer efficiency since a bad misalignment leads to a bad transfer of energy between coils. Although each of the four topologies has its pros and cons, the most used topology in EV is the SS because of two significant advantages [10]. On the SS-compensated topology, the value of the capacitor in the source and receiving sides does not influence

the mutual inductance and does not affect the load conditions, and so the resonant frequencies of the source and receiver sides depend only on the self-inductance of the primary and secondary coils [17] [18] [19]. The other advantage is that the power factor is maintained near one, and so higher efficiencies can be obtained for this compensation topology. In a general way, the four basic topologies are compared in the five following criteria:

1. The maximum efficiency;
2. The maximum load power transfer;
3. The load-independent output voltage or output current;
4. *k*- independent compensation;
5. allowance of no magnetic coupling(*k=0*);

In [20], it was found that the SS is the only compensation scheme that meets all five criteria. The SP was also found to be a suitable compensation alternative. It is also shown that the secondary-series and secondary-parallel compensation schemes are equivalent in terms of efficiency, load power, and component ratings, provided that the quality factor is high. Therefore, the SS and the SP are the most recommended compensation schemes for the IPT system.

To achieve soft-switching in electronic power converts, the primary side of the compensation network is often tuned to make the primary reach zero voltage switching (ZVS) or zero current switching (ZCS) condition [21].

The series and or parallel configurations are added to both sides to create the resonant conditions which are achieved when the energy stored in the capacitor equals the energy stored in the inductor, i.e., when both components have the same impedance [22].To obtain the value of the resonant angular frequency ω_0 is obtained by equaling the inductor impedance to the capacitor impedance of the resonant tank :

$$\omega_0 L_{p,s} = \frac{1}{\omega_0 C_{p,s}} \Rightarrow \omega_0 = \frac{1}{\sqrt{L_{p,s} C_{p,s}}} \tag{8}$$

The linear resonant frequency f_r can also be expressed by the following expression:

$$f_{r(p,s)} = \frac{1}{2\pi\sqrt{L_{p,s} C_{p,s}}} \tag{9}$$

Table 1-Compensations networks advantages and features

Features	Series-Series (SS)	Series-Parallel (SP)	Parallel-Series (PS)	Parallel-Parallel (PP)
Power transfer capability	High	High	Low	Low
The sensitivity of power factor over a distance	Less	Less	Moderate	Moderate
Alignment tolerance	High	High	Moderate	Low
Impedance at resonant state	Low	Low	High	High
Frequency tolerance on efficiency	Low	High	Low	High
Suitable for EV application	High	High	Moderate	Moderate

When the resonance frequency, f_r, of the primary side, *p*, and the secondary side, *s*, are matched together, an efficient power transfer is obtained. When using compensation networks in IPT, the operating frequency ranges from tens of kHz to several hundred kHz, and using this range of frequencies causes a significantly adverse effect on the mutual inductances and hence the reduction of the coupling coefficient [10].

Table 1 shows a comparative analysis of different topologies that are used in WPT for EV [10].

2.6. Challenges and comparisons between topologies

According to [13], a series of WPT challenges regarding efficiency, cost, and health issues can be summarized in Table 2.

Table 2-Challenges of WPT technology.

	Short description	Detailed description
Challenges	Maintenance of dynamic alignment	Lateral alignment for lane-keeping and optimal power transfer coupling for dynamics charging
	Charger life and durability	Need to remain in the road without degrading the structure for at least 20 years and cope with resurfacing works every 10-12years
	Utility power distribution	Connect and distribute the power supply to the point of charging event
	The burden on the electricity grid	Multiple vehicles on charging lane and power flow management
	Synchronization of energizing coils	Low-latency private and secure vehicle-to-infrastructure communication for roadway coil excitation sequencing
	Economic management	Time of use and revenue structure
	Health and safety	Leakage fields: the magnetic and electric fringe fields associated with high-frequency magnetic resonance power transfer
	Tolerance for diverse power demands	Acceptable power levels versus different vehicle class types (car, trucks, busses...)

Table 3 summarizes all the WPT methods mentioned until now regarding performance, price, size/volume, the complexity of the design, power level, and suitability for WEVCS [10].

Table 3-Overview of different methods of WPT.

WPT methods	Performance			Price	Size/ Volume	Complexity of design	Power Level	Suitability for WEVCS
	Efficiency	EMI	Frequency range (kHz)					
Inductive	Medium/High	Medium	10–50	Medium/High	Medium	Medium	Medium/High	High
Capacitive	Low/Medium	Medium	100–600	Low	Low	Medium	Low	Low/Medium
Permanent magnet	Low/Medium	High	0.05–0.500	High	High	High	Medium/Low	Low/Medium
Resonant inductive	Medium/High	Low	10–150	Medium/High	Medium	Medium	Medium/Low	High

The IPC method has been around for some years, but due to lack of investment in the EV market caused by the relatively low prices of fossil fuels, it has not emerged as viable. CPT has gained popularity but only for low power applications since the price and size is mostly amplified compared to the other methods mentioned for higher power applications. PMPT offers low-frequency operation without

compromising that much the power level, and so inherent high-frequency problems do not exist, but there are other concerns as NVH (noise, vibration, and harshness) and lifetime due to the mechanical components used in the transmitter and receivers' sides. Also, cost and size are some factors to be considered when choosing this technology. RIPT methodologies are currently the most used in WPT because they have the best general ratings than the other methods, as shown in Table 3.

2.7. Power of existing WPTS

Table 4 shows some examples of WEVCS prototypes developed by universities at the commercial level [10]. The charging time depends on the source power level, charging pad sizes, and air-gap distance between the two windings. The prices of these prototypes range from 2700 to 13000 USD.

Table 4- Static WEVCS prototypes (Courtesy of C.Panchal et al.).

Research & Development Institute/Corporation	Vehicle Type	Receiver Pad Location	Air-gap distance (mm)	Operating frequency (kHz)	Power Range (kW)	Efficiency (%)
Companies and Start-up Industries						
Plugless Power (Evatran Group) (2016–17)	Passenger car	Front	102	20	3.3 3.6 7.2	90
WiTricy Corporation (2009–17)	Passenger cars and SUVs	ANY	100–250	85	3.6 7.7 11	>90
Qualcomm Halo (2010–17)	Passenger, sport and race car	Center	160–220	85	3.6 6.6 7 20	>90
Hevo Power (2017–18)	Passenger car	ANY	TBA	TBA	10	90
Bombardier Primove (2015–17)	Passenger car to SUVs	ANY	10–30	TBA	3.6 7.2 22	>85
	E-bus	Center			200	
Momentum Dynamic Corporation (2015–17)	Commercial fleet and Bus	Front or Rear	300	TBA	30	TBA
Conductix-Wampfler (2002–03)	Industry fleet and Bus	ANY	TBA	20	up to 20	TBA
Siemens and BMW	Passenger car	Front	80–150	TBA	3.6	>90
Delphi (2011–17)	Passenger car	Front	200	TBA	3.3	TBA
Research Groups and Universities						
Wuhan University, China (2017)	Lab Exp.	N/A	300	100	6–16	~81
Korea Institute of Industrial Technology (KITECH) (2016)	Lab Exp.	N/A	150	85	4	93
Michigan State University (2016)	Lab Exp.	N/A	200	60	1	~82
KAIST University (2016)	Lab Exp.	N/A	200	90	3.3	95.96
Oak Ridge National Lab (ORNL) (2013–17)	Lab & Real Prot.	Rear	100–160	19.5	3.3 6.6 10	~89–90
			125–175	22	20	90
University of Michigan-Dearborn (2014)	Lab Exp.	N/A	200	TBA	8	95.7
University of Auckland (1997–17)	Car	TBA	100–300	10–40	2–5	>85
The University of Georgia (2014–17)	Lab Prot.	N/A	160	20	3	>80
Energy Dynamics Laboratory (EDL) and Utah State University (2012)	Lab Exp.	N/A	152–167	20	5	>90
KAIST University (2010–14)	Car and SUVs	Center	10 120–200	20	3 15	72–80 74–83

2.8. Single-phase full-bridge voltage source converters

Voltage Source Converters (VSCs) are very common for wireless charging applications since most of the power used to charge the vehicles has to be transformed from DC to AC at least one time to supply the batteries inside the vehicle.

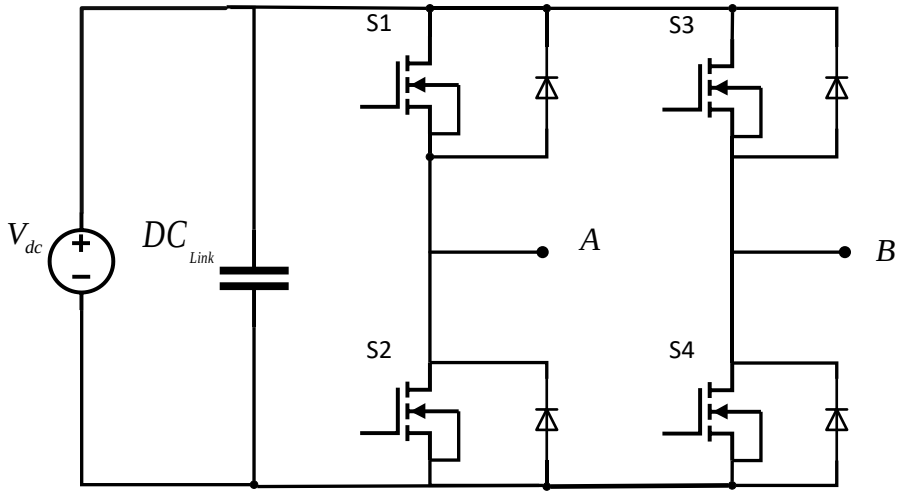

Figure 12-MOSFET single-phase VSC.

Pulse width modulated (PWM) VSCs are the most used power-electronic circuits in practical applications [23]. This type of converter can produce voltages of variable frequency and magnitude. As shown in Figure 12, the single-phase VSC is a full bridge or H-bridge topology.

The output voltage switches between V_{DC} and $-V_{DC}$ depending on which pair of transistors are conducting. The possible combination is:

- When *S1* and *S4* are switched ON, the voltage and the output are equal to V_{DC}.
- When *S2* and *S3* are switched ON, the output is equal to $-V_{DC}$.

The Fourier series of the output voltage v_{ab} is given by the following expression:

$$v_{ab} = \frac{4V_d}{\pi}\left(\sin(\omega t)+\frac{1}{3}\left(\sin(3\omega t)+\frac{1}{5}\left(\sin(5\omega t)+...\right)\right)\right) \quad (10)$$

Where ω is the fundamental angular frequency ($\omega = 2\pi f$). From equation (10), it is possible to write the peak and RMS value of the fundamental component of the output voltage as $V_{ab1} = \frac{4V_d}{\pi}$ and $V_1 = \frac{V_{ab1}}{\sqrt{2}}$.

It is essential to relate the output current of the VSC and the current at the transistors. This relation is crucial when accounting for the losses resulting from the switching between off and on the transistors' states. It is essential to consider this calculation when performing the semiconductor selection to ensure this has the characteristics to conduct the currents and voltages.

The relation between the RMS value of the current in the transistor I_{SRMS}, and the AC current I_{RMS} in the VSC is:

$$I_{Srms} = \frac{I_{RMS}}{\sqrt{2}} \tag{11}$$

The current that flows through the transistor at the switching moment is also essential to consider since it is correlated to the switching losses a well. This current has its maximum value at:

$$I_{S\max} = I + \Delta i_0 \tag{12}$$

Where Δi_0 is the maximum ripple current.

2.9. Zero voltage switching (ZVS) and Zero current switching (ZCS)

WPT systems require power converters such as rectifiers and inverters, to enable the charging process. The topologies used for the power converters require semiconductors such as MOSFET's, IGBT's, Diodes or, at higher switching frequencies, wide bandgap semiconductors as SiC (Silicon Carbide) MOSFETs or GaN HEMTs (Gallium Nitride, High Electron Mobility Transistors). Power switches have to turn-on and turn-off depending on if it is required or not to feed the load under hard-switching conditions. Hard switching refers to the stressful switching behavior of the power electronic devices [24]. The switching trajectory of a hard-switched power device can be seen in Figure 13.

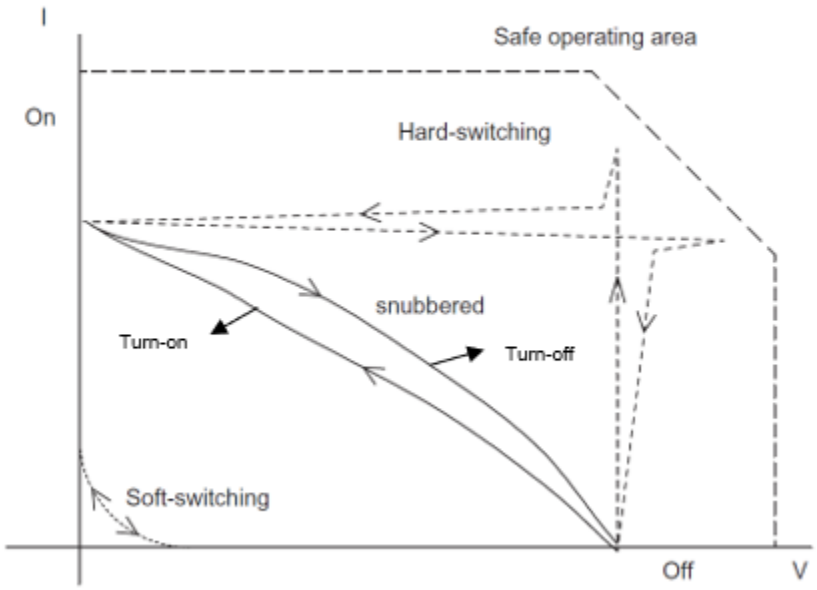

Figure 13-Typical switching trajectories of power switches (Courtesy of M.H. Rashid et al.).

During this hard switching, the power device has to withstand high voltage and current, resulting in high switching losses and stress. It is possible to have dissipative elements to reduce these switching losses, as shown in Figure 13, where a snubber circuit (consisting of passive elements) is used to dissipate some of the energy resulting from the hard switching. However, this approach results in switching power losses from the switch to the snubber, and as a result, the overall efficiency decreases. There is another factor to be considered that is the power devices switching frequency. The higher the switching frequency, the higher the switching losses.

To overcome this problem regarding the switching losses, resonant converters are used. Resonant converter includes a resonant tank, with an LC circuit operating at resonance frequency, to create oscillatory voltage and/or current waveforms so that ZVS and ZCS conditions occur. This resonant tank is also used to store, and transfer energy from the input to the output in a manner similar to the conventional resonant converter [25].

The ZCS operation consists of shaping the device's currents using the resonant tank at on-time to create zero-current conditions for the device to turn off. In ZVS the voltage waveform is shaped so that at the off-time the device is in zero-voltage conditions to the device to turn on.

Resonant converters can be categorized as follows:

- Load-resonant converters
- Resonant-switch converters
- Resonant-dc-link converters
- High-frequency-link integral-half-cycle converters

The load-resonant converter uses an LC resonant tank where either a series LC or a parallel LC circuit can be implemented. By applying an oscillating voltage and current, converters will switch at zero voltage and/zero current thanks to the resonant tank. The tank impedance controls the power that flows to the load. This impedance is obtained by comparing the switching frequency with the resonant frequency of the tank.

Resonant-switching converters or quasi-resonant converters can also be used to provide ZVS and ZCS, but unlike the load-resonant converters, they can act as resonant converters during one switching-frequency period and as non-resonant during another time interval.

Resonant-dc-link converters are different from pulse width modulation(PWM) dc-ac converters, where a dc signal is converted to a sinusoidal output by using a sinusoidal pulse width modulation strategy. In the resonant-dc-link converters, the input voltage oscillates by using an LC resonant tank so that the input voltage remains zero for a finite duration creating ZVS conditions.

Finally, the High-frequency-link integral-half-cycle converters are based on bidirectional switching where the input of an inverter (single or three-phase) is a high-frequency sinusoidal ac signal. It is possible to synthesize a low-frequency ac signal with a variable magnitude and frequency of an adjustable magnitude dc signal, where the switches are turned on and off at the zero crossings of the input voltage [26].

To understand how a load-resonant converter uses the LC tank to apply zero voltage and current switching, a half-bridge configuration is shown in Figure 14 [26]. When using a Series-Loaded Resonant dc-dc Converter, the resonant tank is formed by L_r and C_r.

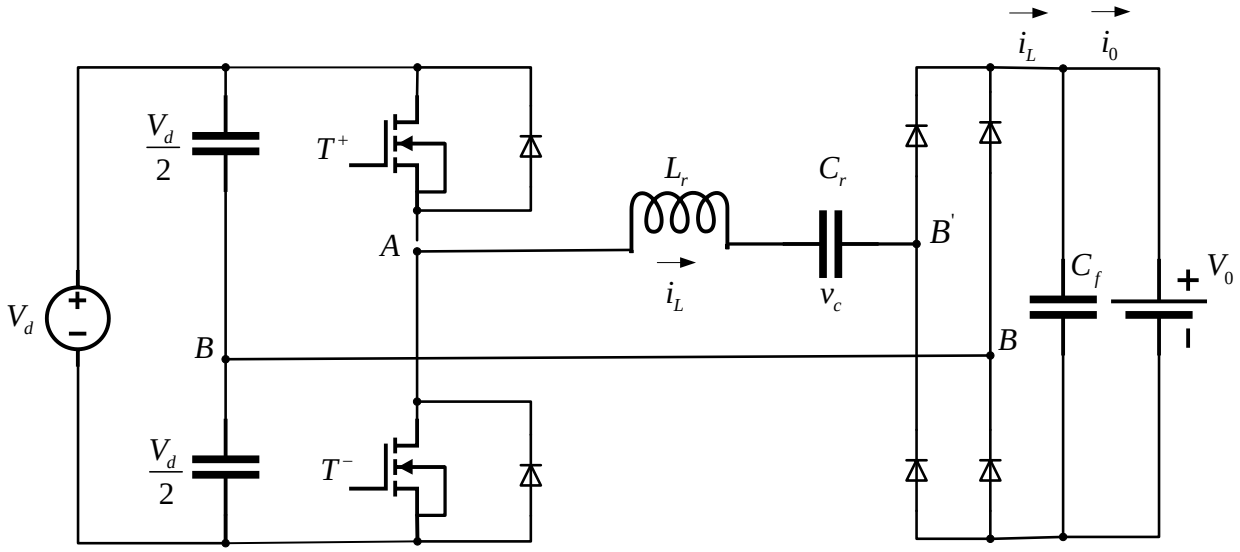

Figure 14-SLR dc-dc half-bridge converter.

On this representation of an SLR dc-dc converter, it is represented the full-wave current rectified at the output $|i_L|$. The output voltage V_0 is reflected across the rectifier input as $v_{A'B}$. If i_L is positive, $v_{B'B} = V_0$ and $v_{B'B} = -V_0$ for negative i_L.

When the current in the inductor is positive, this means that the switch T_+ will be ON; otherwise, the conduction is made by the diode D_-. For negative values of the current i_L, T_- and D_+ acts similarly. The voltage v_{AB} applied across the tank is:

For i_L>0:

$$\begin{aligned} T_+on: v_{AB} &= +\frac{1}{2}V_d; v_{AB'} = +\frac{1}{2}V_d - V_0 \\ D_+on: v_{AB} &= -\frac{1}{2}V_d; v_{AB'} = -\frac{1}{2}V_d - V_0 \end{aligned} \tag{13}$$

For $i_L < 0$

$$\begin{aligned} T\_on: v_{AB} &= -\frac{1}{2}V_d; v_{AB'} = -\frac{1}{2}V_d + V_0 \\ D_+on: v_{AB} &= +\frac{1}{2}V_d; v_{AB'} = +\frac{1}{2}V_d + V_0 \end{aligned} \tag{14}$$

The voltage v_{AB} applied across the tank depends on which semiconductor is conducting and the direction Figure 15 [26], where the equations (13) and (14) are applied.

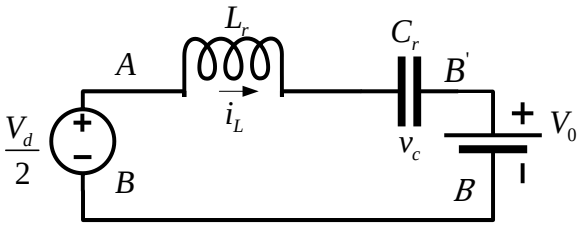

Figure 15-Equivalent Circuit of SLR dc-dc half-bridge converter.

The output voltage cannot exceed the input voltage,that is, $V_0 \leq \frac{1}{2}V_d$.There are three possible modes of operation based on the ratio of the switching frequency ω_s to the resonance frequency $\omega_0 = \frac{1}{\sqrt{L_r C_r}}$. This ratio determines if i_L flows continuously or discontinuously.

The first mode considered is the DCC, with $\omega_s < \frac{1}{2}\omega_0$. Because of the discontinuous interval where the current i_L remains zero one half-cycle of the operating frequency exceeds 360º of the resonance frequency. In this mode of operation, the switches turn off naturally at zero current and zero voltage since the current i_L goes through zero. The problem is that when the switches turn on, there is also zero current, but not zero voltage, and the same happens for the diodes. The main disadvantage is the relatively large peak current in the circuit, causing higher conduction losses than the CCM.

On CCM, there are two different modes, one when $\frac{1}{2}\omega_0 < \omega_s < \omega_0$ and another when $\omega_0 < \omega_s$. Regarding the first CCM, both T and D conducts for less than 180º. The switches turn on at a finite current and a finite voltage resulting in turn-on switching losses. However, the turning-off occurs naturally at zero current and zero voltage. In this last mode, with $\omega_0 < \omega_s$ the switches are forced to turn off at a finite current, but they are turned on at a zero current and voltage. The combined conduction intervals for T_+ and D_- is equal to one half-cycle of operation at the switching frequency of ω_s. This half-cycle is less than 180º of the resonance frequency ω_0 resulting in $\omega_0 < \omega_s$. The main advantage of operating in this mode is that the switches turn on zero current and zero voltage. The main disadvantage is that the switches need to force turn off near the peak of i_L, causing a large turn-off switching loss that can be partly overcome by using lossless snubber capacitors in parallel with the switches.

Besides the SLR converter, the parallel-loaded resonant dc-dc converters, PLR, where the LC tank appears connected parallel with the output stage, is also a reliable solution. [26].

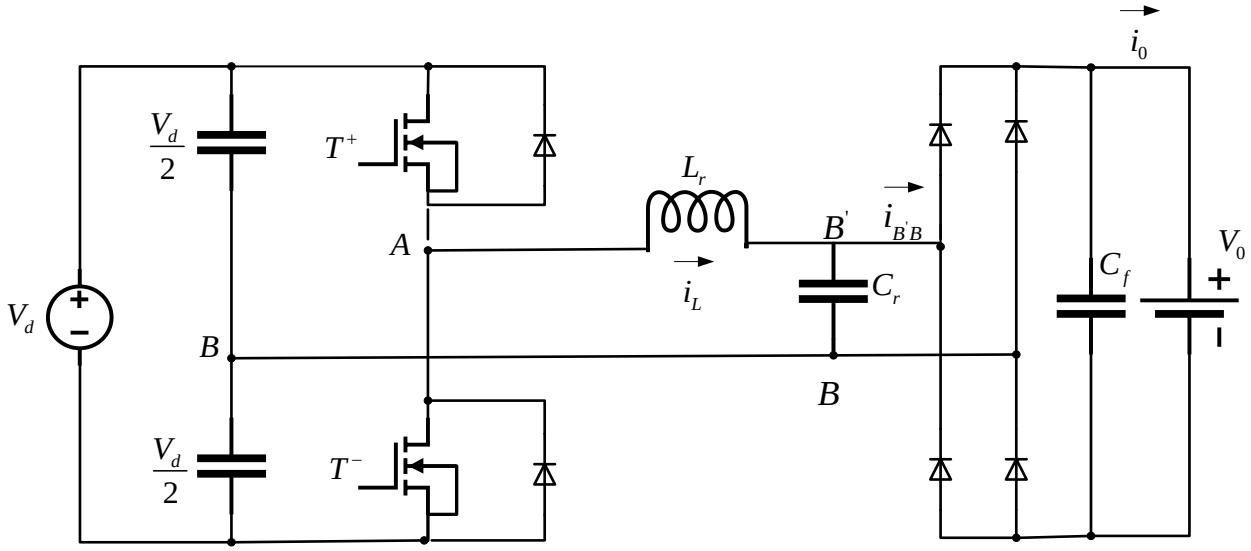

Figure 16-PLR dc-dc half-bridge converter.

The PLR converters, in comparison with the SLR converters, differ in the following aspects:

1. PLR converters appear as voltage sources and hence, are better for multiple outlets;
2. PLR converters do not have an inherent short-circuit protection capability, and this is a drawback when compared with the SLR topology;
3. PLR converters can be used as a step-up and step-down converter, meaning that they produce higher or lower voltage levels at the output, while the SLR can only act as a step-down converter.

The voltage across the capacitor C_r is rectified, filtered, and supplied to the load. This voltage is represented in Figure 16 as v_{AB}. The value of v_{AB} depends on which device is conducting:

$$T_+ \ or \ D\_on: v_{AB} = +\frac{1}{2}V_d$$
$$T_- \ or \ D_+on: v_{AB} = -\frac{1}{2}V_d \quad (15)$$

As it was done for the SLR, an equivalent circuit can be obtained.

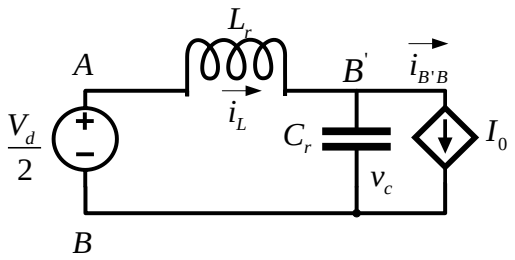

Figure 17-Equivalent circuit of PLR dc-dc half-bridge converter.

The current $i_{B'B}$ direction depends on the polarity of the voltage v_c across the resonant tank that depends on which switch is turned on. The PLR dc-dc converter can operate in many different combinations of the states of i_L and v_c. Only three modes are going to be mentioned. DCM, CCM with $\omega_0 > \omega_s$ and CCM with $\omega_0 < \omega_s$.

For the first case, DCM, not only i_L remains at zero for some length of time but also v_c remains at zero simultaneously. The interval where both $i_L$and v_c are zero can be varied to control the output voltage. There are no turn-on or turn-off stresses or losses on the switches or the diodes.

In CCM with $\omega_0 > \omega_s$, both $i_L$and v_c are continuous. The switches turn on at a finite i_L.This results in turn-on losses in the switches. But there are no turn-off losses in the switches since the current that goes through them commutates naturally when i_L reverses direction.

In CCM with $\omega_0 < \omega_s$, as in the previous case both $i_L$and v_c are continuous. And contrary to when the $\omega_0 > \omega_s$ there are no turn-on losses since they switch on when the current naturally reverses, but this results in turn-off losses since the switch is forced to turn off when the current is not zero. As it was done for the SLR converter, it is possible to eliminate the turn-off losses by connecting a lossless snubber consisting of a capacitor in parallel with each switch.

3. Simulation of an IPTS for EV charger

A flowchart is presented in Figure 18 with the steps that were followed when designing the IPTS prototype. A detailed explanation is also given on how each charger's component was selected and how the system's control was implemented.

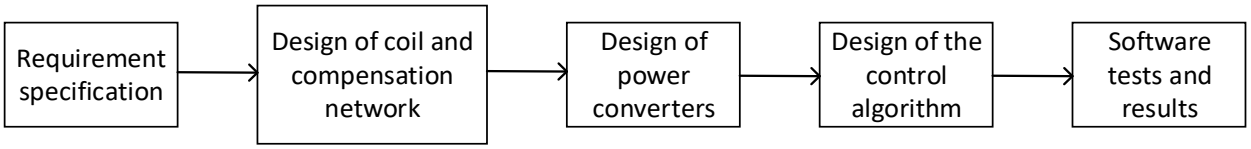

Figure 18-Flowchart for the design of the IPT charger.

The main goal is to prove the importance of having a compensation network to improve the inductive charger's general power transfer capability while using the principle of resonant inductive coupling.

Before designing the prototype, it is essential to define which of the main requirements for the IPT. The requirements specifications are as follow:

- The power supplied to the generic load is 100 W.
- The supply grid has a nominal 230 V and a frequency of 50 Hz.
- The nominal voltage at the generic load is 15 V.
- Simple control algorithm.
- Capacity for bidirectional power flow if any V2G was to be used.
- The opted operational frequency for this application is 150 kHz.

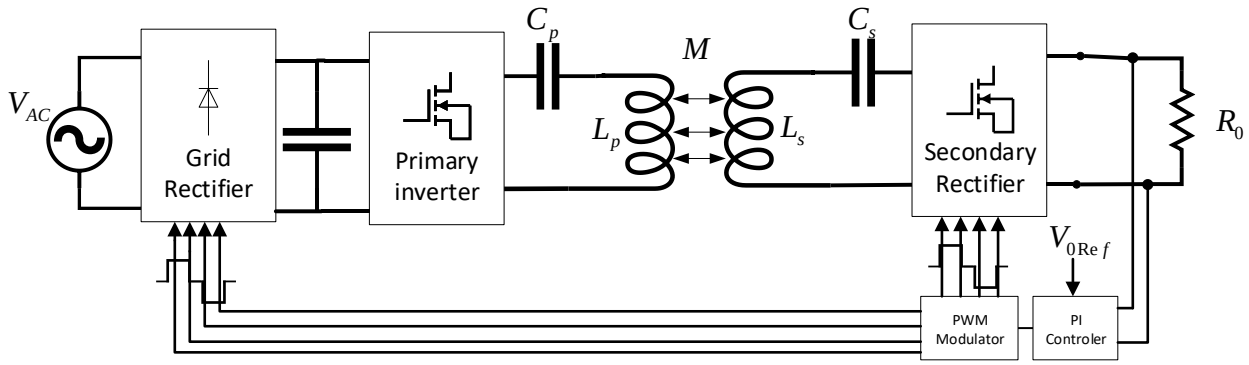

Figure 19-Topology of the wireless charger.

3.1. Design of the coils and Compensation Network

One of the leading causes of low efficiencies is the weak coupling due to the large leakage inductance in both sides of the IPT Transformer. A simplified equivalent circuit of the IPT is shown in Figure 20.

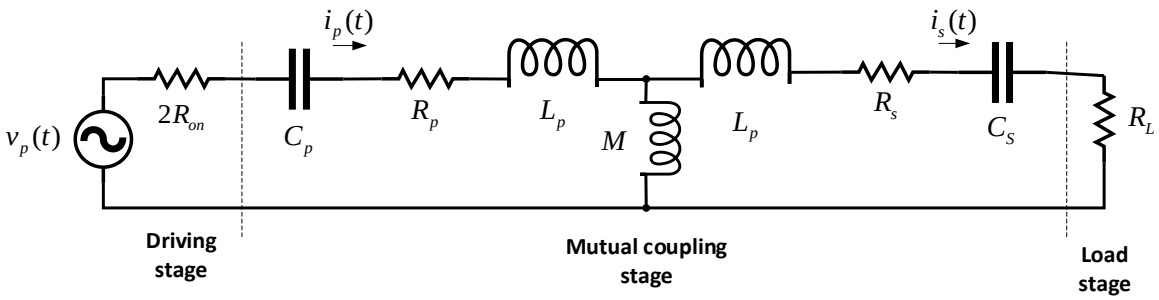

Figure 20-IPT equivalent circuit.

The equivalent model is divided into three parts. The driving stage represents the AC source, v_P, plus a conduction resistance, R_{ON}, of any converter that may appear before the IPT. The mutual coupling stage is modeled using a T-network. The resistance of the primary coil and secondary are represented by R_P and R_S. The resistance represents the load R_L. *M* is the mutual inductance between the two coils, which is related to *k* and the primary and secondary self-inductances L_P and L_S as it is shown in equation (6).

An inductance is associated with the uncoupled flux or leakage flux called leakage inductance on typical transformers [27].

The leakage inductances on the primary and secondary sides, L_{Pk} and L_{Sk} are expressed as a function of *k*:

$$L_{Pk} = (1-k)L_P$$
$$L_{Sk} = (1-k)L_S \quad (16)$$

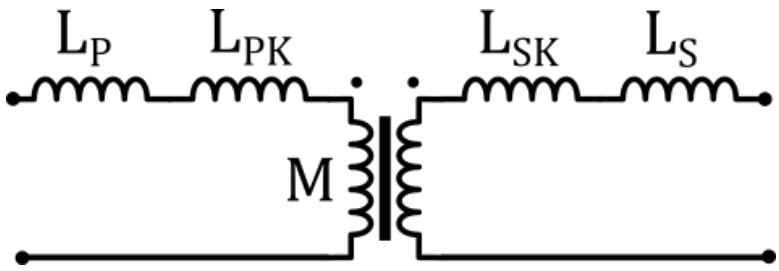

Figure 21- Leakage, self, and mutual inductance in a winding pair

Figure 21 illustrates the leakage inductance on an electric circuit with a coupled pair of windings in a transformer. The leakage inductance always appears as a series element, and it does not matter where the inductance is paced for modeling purposes since its electrical behavior is the same.

The primary and secondary resonant circuits are designed to resonate at the same frequency. The resonance frequency is given by (9). When the circuit is driven at the resonance frequency on both sides, the primary and secondary sides' leakage reactance is canceled out by the capacitive reactance. Thus, by introducing a compensative network with the capacitors C_P and C_S the overall efficiency of the charging process is expected to increase.

As mentioned before, the coil design has a significant effect on the overall efficiency of the charging process. Factors such as the dimensions, weight, material, and the number of coils should be well analyzed. But since this simulation aims to prove the overall superior efficiency of using a compensation network, a 1:1 system of coils is used. The primary and secondary coil are the same with all the specifications given in the datasheet [28] supplied by Wurth Elektronik.

Table 5-Properties of the wireless coil

Property	$L_p\,(\mu H)$	$L_s\,(\mu H)$	$M\,(\mu H)$
Value	5.8	5.8	2.9

The properties of the wireless coil are defined in Table 5. The value of mutual inductance M is defined by the equation (6), considering the coupling factor, k, equal to 0.5.

The compensation network selected is the series-series topology since, as it was previously mentioned, it is the most popular of all the topologies mentioned before. The sizing of the capacitors is derived from the equations (8) and(9) which by assuming that the tank, composed of the compensation capacitor and the wireless inductor at each side of the charger, working at 0.9 of the operational frequency, $f_o = 135\ kHz$.The following expression can be deduced to arrive in the value of each capacitor:

$$C_p = \frac{1}{L_p \omega_0^{\,2}} = 48nF \tag{17}$$

$$C_s = \frac{1}{L_s \omega_0^{\,2}} = 48nF \tag{18}$$

The resonant tank diagram is illustrated in Figure 22. A two winding linear transformer block with a turn ratio of 1:1 is used, where the values of the winding resistances were 1 % of the total losses on the transformer. Both windings have a series-series topology, i.e., the compensations capacitor are in series with the winding inductance.

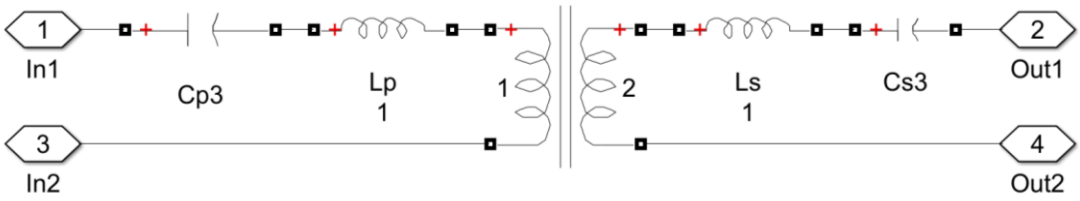

Figure 22- Resonant block

3.2. Design of the Power Converters

The proposed topology, illustrated in Figure 23, comprises two power converters: a single-phase full-bridge inverter on the primary side and a single-phase full-bridge rectifier on the secondary side.

The primary inverter is essential to control the amount of power transferred to the resonant tank. This power converter's design was implemented with the Simulink block “MOSFET/DIODE,” as illustrated in Figure 23 and Figure 24. The diodes placed in parallel with the MOSFET provides the possibility of performing V2G applications since it allows current to have a direction from the charge to the grid.

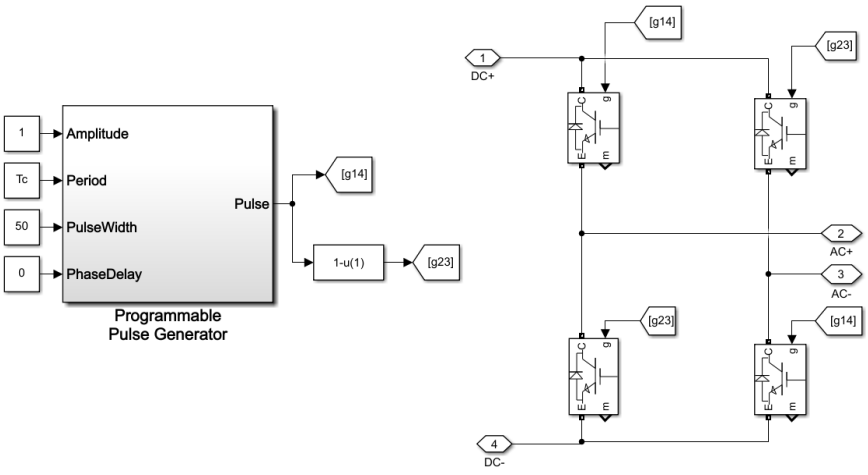

Figure 23- Inverter topology.

The secondary side's rectifier converts the AC signals coming from the resonant tank to a controlled DC voltage used to supply the load. The same concept of placing a diode in parallel with the MOSFET was used.

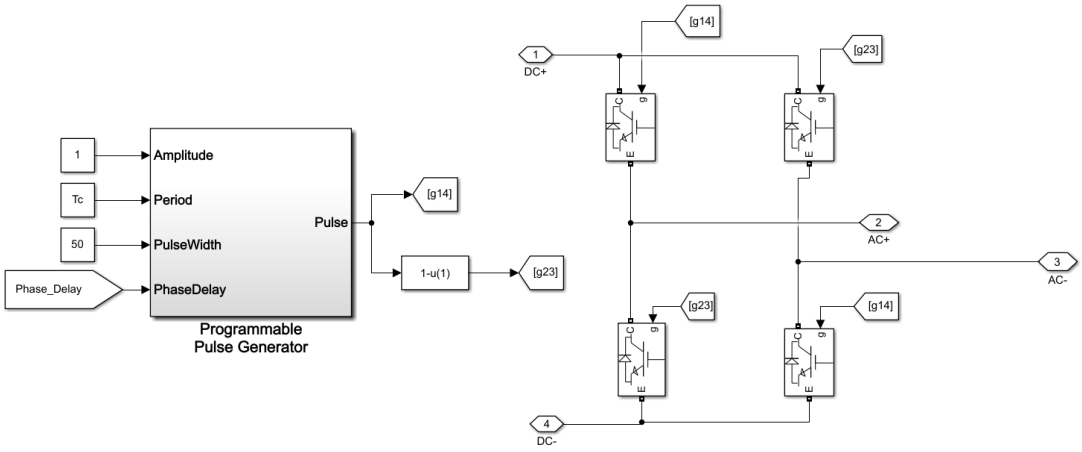

Figure 24- Rectifier topology.

3.3. DC-Link Capacitance

A DC link capacitance is used to control voltage ripples and ensure a low inductance current path for high-frequency currents derived from VSC switching. The capacitor acts as a storage of DC energy and filters out the variation of the DC voltage. This capacitor serves as a connection between the grid rectifier, externally connected to the PCB, to the primary VSC.

This capacitor needs to be sized according to specifications for the ripple voltage. It takes into consideration the maximum current that is expected to go through the capacitor. The current is an important parameter to analyze when designing capacitors since they have limits for the maximum currents they can handle. Finally, they must also handle high current transient generated from the switching between states of the semiconductors on the converters. Assuming a ripple of 1% of the DC voltage, ΔV_{DC}, and a current ripple, Δi, of 20 % of the DC link can be sized in the following way [29]:

$$C = \frac{\Delta i T}{4\Delta V_{DC}} = \frac{0.2 \times I_{peak}}{4 \times 0.01 V_{DC} f_{sw}} = \frac{0.2 \times 12.5}{4 \times 0.01 \times 15 \times 1500000} = 28 \mu F \quad (19)$$

According to [30], it is essential for DC-link capacitors design and selection in VSCs since it contributes to the cost, size, and failure rate on a considerable scale.

3.4. Controller design

The control algorithm was implemented in the secondary converter to regulate the power transfer. The converter controller was designed so that the phase between the primary and secondary voltage waveforms ensures a specific load voltage through the charging process.

This controller measures the voltage being applied to the load to determine the phase shift and control the transistor switching to implement the phase shift.

Figure 25 shows the overall control scheme. The power converter is modeled with a gain, K_D, and a time delay, T_d . The voltage error is obtained by a reference voltage, V_{0Ref} , and the measurement of the output voltage, V_0 where alfa is a gain based on the instrumentation setup. The desired controller, C(s), gives as output the phase difference given by $\sin\delta$, such that the error is 0.

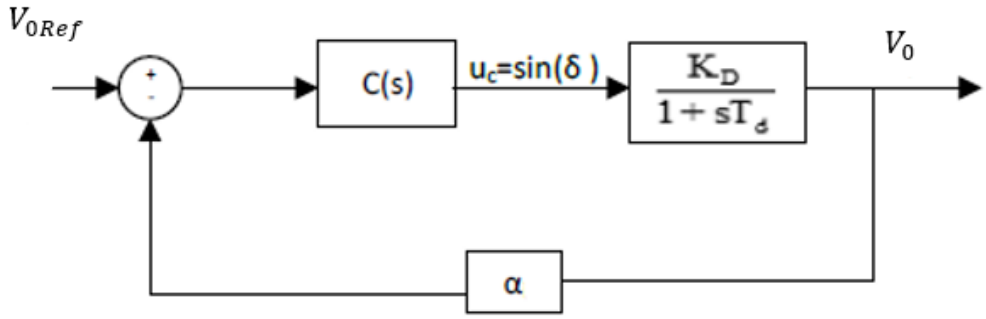

Figure 25- Equivalent control scheme.

To design the controller C(s), it is necessary to establish the relation between the power received from the resonant tank, P_{in} . And the power delivered to the load, P_0. In this expression, it is assumed that there are not any power losses at the converter:

$$P_{in} = P_0 \tag{20}$$

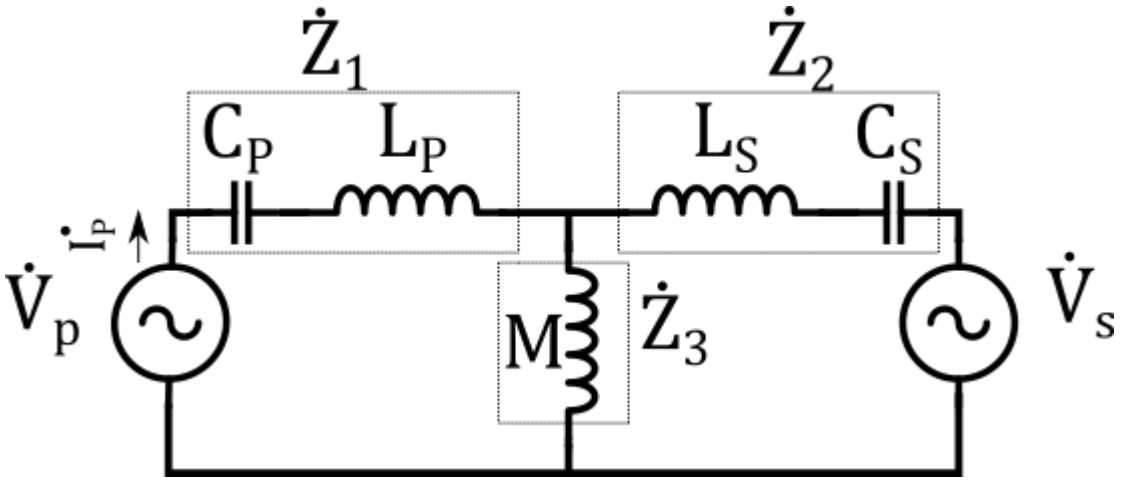

Figure 26-Simplified equivalent circuit of the resonant tank

To express P_{in} , a simplified equivalent circuit of the resonant tank is illustrated in Figure 26. The voltages source $\dot{V}_p$ and $\dot{V}_s$, which represent the primary and the secondary voltage of the resonant circuit, respectively, can be denoted concerning the phase angle δ as:

$$\dot{V}_p = V_p e^{j0} = V_p \tag{21}$$

$$\dot{V}_s = V_s e^{-j\delta} = V_s \cos\delta - jV_s sin\delta \tag{22}$$

The impedances represented in Figure 26 can be expressed by:

$$\dot{Z}_1 = j\left(X_{L_P} - X_{C_P}\right) = \left(X_{L_P} - X_{C_P}\right)e^{j\frac{\pi}{2}} \tag{23}$$

$$\dot{Z}_2 = j\left(X_{L_S} - X_{C_S}\right) = \left(X_{L_S} - X_{C_S}\right)e^{j\frac{\pi}{2}} \tag{24}$$

$$\dot{Z}_3 = jX_M = X_M e^{j\frac{\pi}{2}} \tag{25}$$

The reactances from the equations (23)(24)(25) of each reactive component can be written as:

$$X_{L_P} = \omega L_P, X_{L_S} = \omega L_S, X_M = \omega M \tag{26}$$

$$X_{C_P} = \frac{1}{\omega C_P}, X_{CS} = \frac{1}{\omega C_S} \tag{27}$$

The current from the primary side $\dot{I_p}$ can also be expressed by:

$$\begin{aligned}\dot{I}_P &= \frac{(Z_M + Z_2)V_p - Z_M V_s e^{-j\frac{\pi}{2}}}{Z_M(Z_1 + Z_2) + Z_1 Z_2} \\ &= \frac{X_M V_s \sin\delta}{\Gamma} - j\{\frac{X_M V_p - (X_M + (X_{L_P} - X_{C_1}))V_s - X_M V_s \cos\delta}{\Gamma}\}\end{aligned} \tag{28}$$

$$\Gamma = X_M\left\{\left(X_{L_P} - X_{C_P}\right) + \left(X_{L_S} - X_{C_S}\right)\right\} + \left(X_{L_P} - X_{C_P}\right)\left(X_{L_S} - X_{C_P}\right) \tag{29}$$

It is possible now to arrive at the expression of the active power that is being transferred from the resonant tank to the converter:

$$\begin{aligned}P_{in} &= \mathrm{Re}(\dot{V}_p \dot{I}_p) \\ &= \frac{X_M V_p V_s}{\Gamma}\sin\delta\end{aligned} \tag{30}$$

The expression of the power transferred to the battery, P_0 , can be written only as:

$$P_0 = I_0 V_0 \tag{31}$$

Finally, since $V_p = V_s = V$ it is possible to obtain the following relation:

$$V_0 = \frac{X_M V^2}{\Gamma I_0}\sin\delta \tag{32}$$

Since the controller is designed to have on his output $\sin\delta$, from the equation (32), the gain of the system K_D is:

$$Kd = \frac{X_M V^2}{\Gamma I_0} \tag{33}$$

The control block subsystem used in the simulation is illustrated in Figure 27. The relation between the voltage on the load and the reference voltage is made using a soft-starter so that the results don't have any discontinuities avoiding any possible situation of instability by the controller at the beginning of the simulation. The controller uses the error between the load voltage and the reference voltage, and a phase-shift is applied between the primary and the secondary converter waveforms.

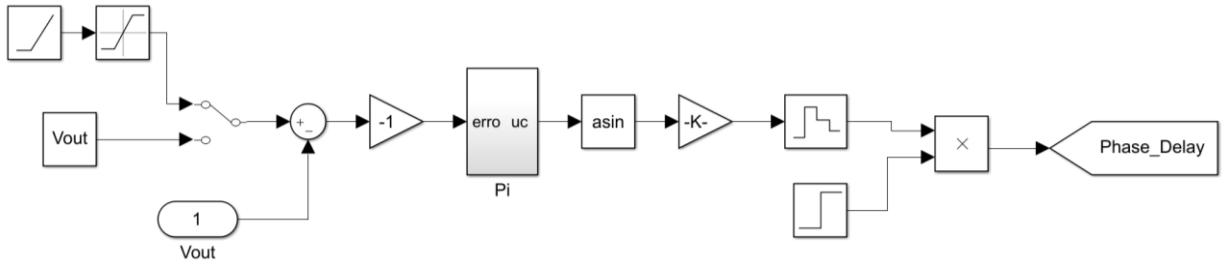

Figure 27- Control system implementation using the Simulink software.

The control system was implemented using a proportional and integral or PI-control configuration to implement the phase shift. The PI controller is a ubiquitous controller in industrial control systems [31] . Both gains have different effects on the controller. The proportional gain provides stability and high-frequency response, while the integral gain ensures that the average error reaches zero. An anti-windup technique was also used to prevent overshoots by the PI-controller's integrator, as illustrated in Figure 28. The PI control function can be expressed as:

$$C(s) = \frac{u_c(s)}{V_{0\mathrm{Re}f}(s) - V_0(s)} = K_p + \frac{K_i}{s} \tag{34}$$

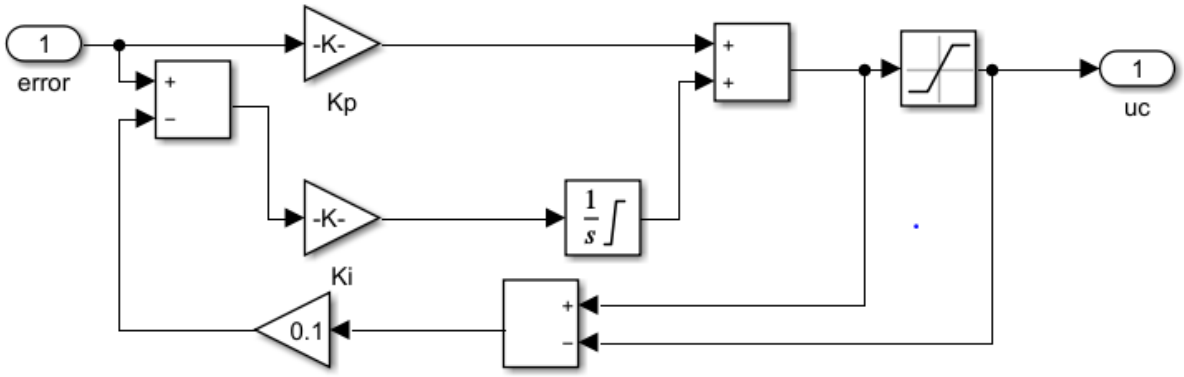

Figure 28- PI controller.

Attending the system control in the closed-loop transfer function of the control system is given by:

$$\frac{V_0(s)}{V_{0\mathrm{Re}f}(s)} = \frac{\frac{K_p s + K_i}{s}\frac{K_d}{1+sT_d}}{1+\frac{K_p s + K_i}{s}\frac{K_d}{1+sT_d}\alpha} = \frac{K_d(K_p s + K_i)}{s^2 T_d + s(1+K_d K_p \alpha) + K_d K_i \alpha} = \frac{1}{\alpha}\frac{\frac{\alpha K_d K_i}{T_d}(\frac{K_p}{K_i}s+1)}{s^2 + s\frac{1+K_d K_p \alpha}{T_d} + \frac{K_d K_i \alpha}{T_d}} \quad (35)$$

Applying the final value theorem to the closed-loop transfer function in (35), a steady-state error is arrived by the system amplified by the gain$\frac{1}{\alpha}$.

$$\lim_{s\to 0}\frac{V_0(s)}{V_{0\mathrm{Re}f}(s)} = \frac{1}{\alpha} \quad (36)$$

Comparing the expression(35) to the 2^{nd} order canonical form:

$$G_{2^{nd}}(s) = \frac{{\omega_n}^2}{s^2 + 2\xi\omega_n s + {\omega_n}^2} \quad (37)$$

The proportional gain Kp and integral gain Ki are given by the following expressions:

$${\omega_n}^2 = \frac{K_d Ki\alpha}{T_d} \Rightarrow Ki = \frac{T_d {\omega_n}^2}{K_d \alpha} \quad (38)$$

$$2\xi\omega_n = \frac{1+K_d K_p \alpha}{T_d} \Rightarrow Kp = \frac{2\xi\omega_n T_d - 1}{K_d \alpha} \quad (39)$$

The expression gives the natural frequency:

$$\omega_n = \frac{(\alpha_z \xi)}{(T_d(2\alpha_z \xi^2 - 1)^2)} \quad (40)$$

Where T_d is the statistical delay of the converter given by $T_d = T_{sw}$ and α_z is an adjustable gain. The damping coefficient ξ is equal to $\frac{\sqrt{2}}{2}$ to restrict any oscillations on the output of the controller.

4.Simulation Results

This section presents a single-phase computational IPT model, illustrated in appendix A, to simulate a generic load's charging process dynamically.

Based on the results, conclusions were drawn on the charging process performance. All simulations were made using the software Simulink and MATLAB [32].

To validate the proposed topology and controller some software tests need to be performed to evaluate if the model is behaving according to what is expected.

As illustrated in Appendix A- Simulink Simulation, each part of the model is implemented with blocks. The grid is rectified by a diode bridge and then by using a capacitor to smooth the voltage applied to the primary VSC before reaching the resonant tank. The voltage coming from the resonant tank is then rectified and applied to a capacitor to minimize the voltage ripple once again before being applied to the load.

The control block is not directly connected to the rest of the model but receives the voltage at the load terminal so that phase shift control can be implemented.

Some measurement blocks are used to measure the voltage and current waveform on each part of the model between the power converter blocks and the resonant tank.

Since the VSC was implemented using 4 MOSFET in a full-bridge topology, the MOSFET block allows measuring each device's electrical magnitudes, such as the voltage applied to the semiconductor and the instantaneous current.

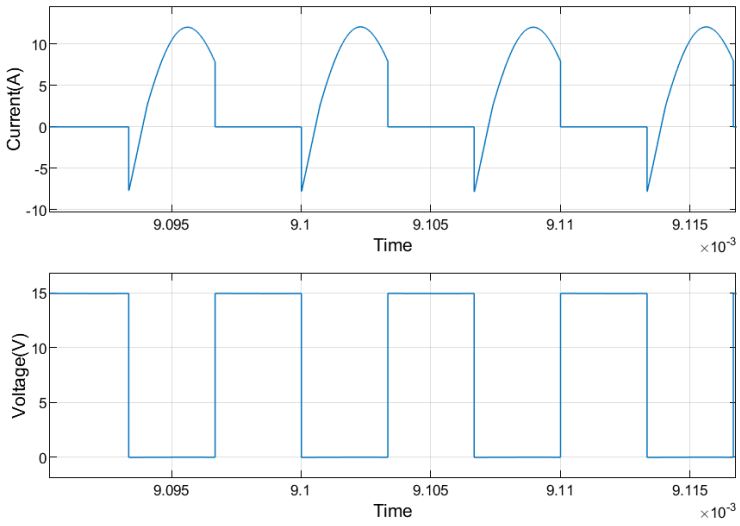

Figure 29- Current and voltage measurements on the MOSFET (primary VSC).

The voltage and current waveforms on the resonant tank were measured in the same scope. Figure 30 illustrates the phase-shift between the voltage at the primary and secondary sides of the tank and shows that the currents on each side are in phase with their corresponded voltages, which means the power being transferred is mainly active, which was one of the main requirements that were intended.

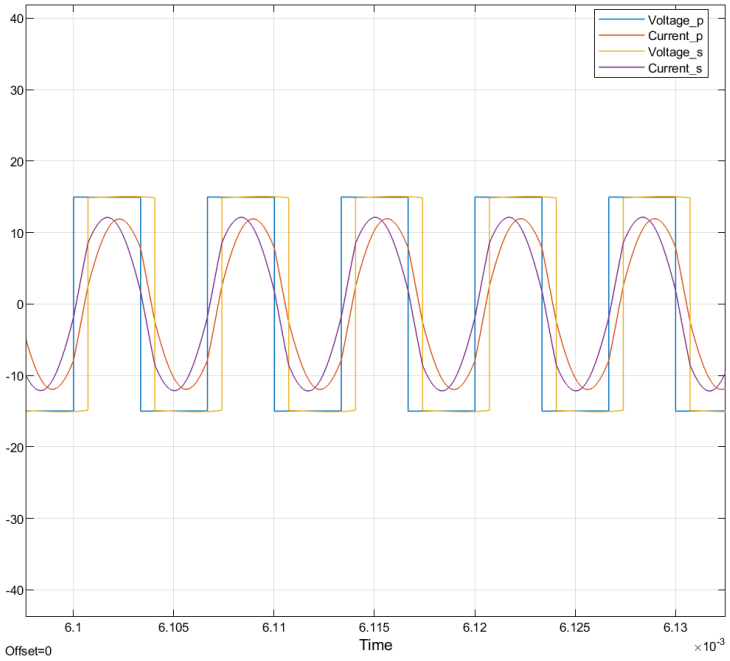

Figure 30- Waveforms on the resonant tank.

The converter after the resonant tank was also implemented by using 4 MOSFETs and so it is possible to measure the electrical magnitudes of each device, such as the voltage applied to the semiconductor and the instantaneous current(Figure 31).

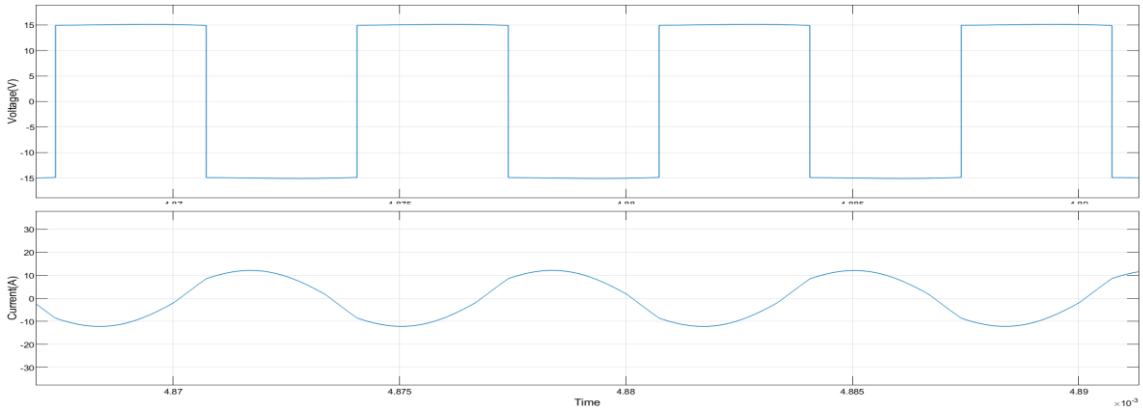

Figure 31- Voltage and current measurements on the MOSFET (converter VSC)

Regarding the controller, Figure 32 illustrates the error between the load voltage and the reference voltage. It is possible to observe a correct tracking of the reference value with a small voltage ripple around the reference voltage. The error stays near zero until the end of the charging process.

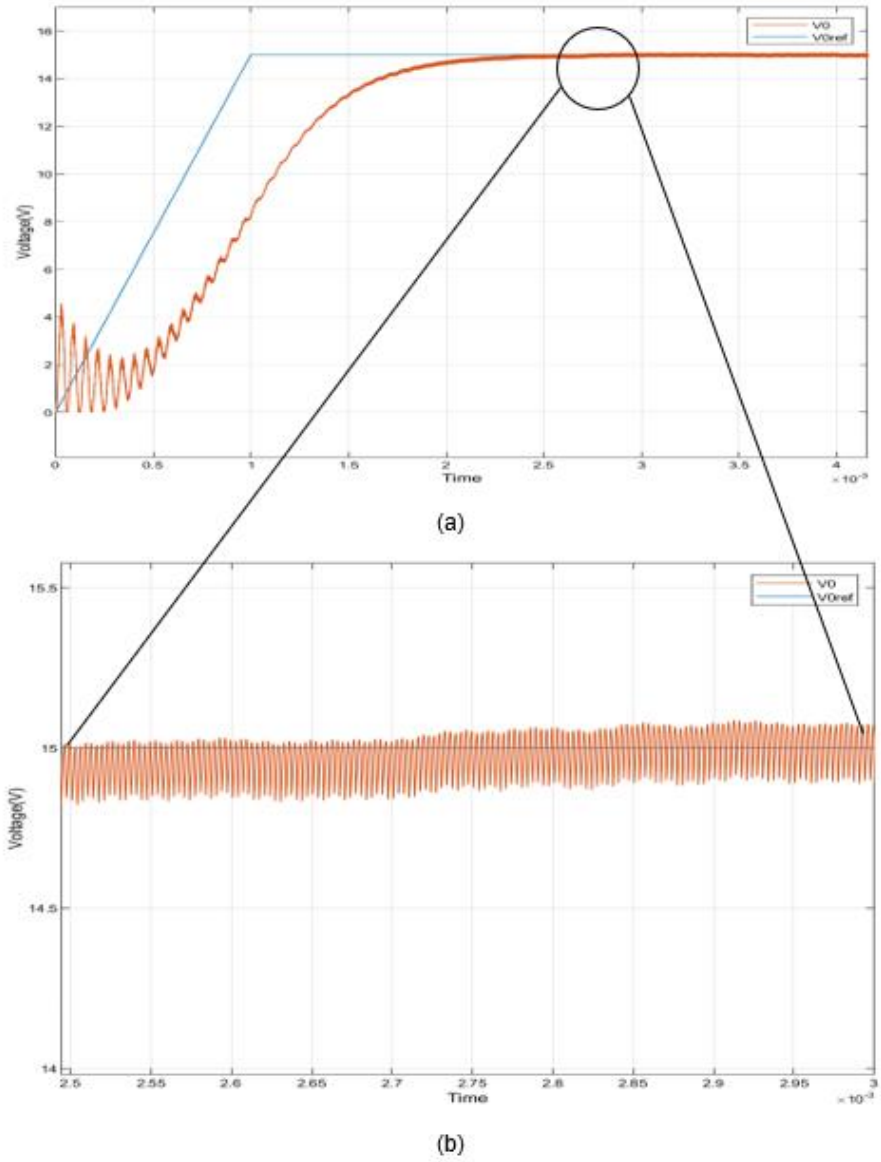

Figure 32-a) Voltage applied to the load, V_0, and reference value of voltage, V_{0Ref};b) Zoom between 2 and 3 ms to illustrate the error between the reference and the load voltage.

After the secondary rectifier, a filter block containing a capacitor allows removing AC components remaining at the converter's output signal, reaching an almost purely dc signal to the load. This capacitor value can be calculated, for a 1% output voltage ripple target, by the following expression [29]:

$$C_0 = \frac{I_0}{2\pi f_{sw} 0.01 V_0} \tag{41}$$

Figure 33 shows the voltage and current applied to the load, which is purely resistive. A transient can be seen in this figure, on which the voltage at the beginning of this simulation is reaching the desired value of 15 V. The transient is controlled by sizing the parameters such as the proportional gain Kp and integral gain Ki so that the transient is not too long. The same transient can be detected in Figure 34 of the power measurement at the load.

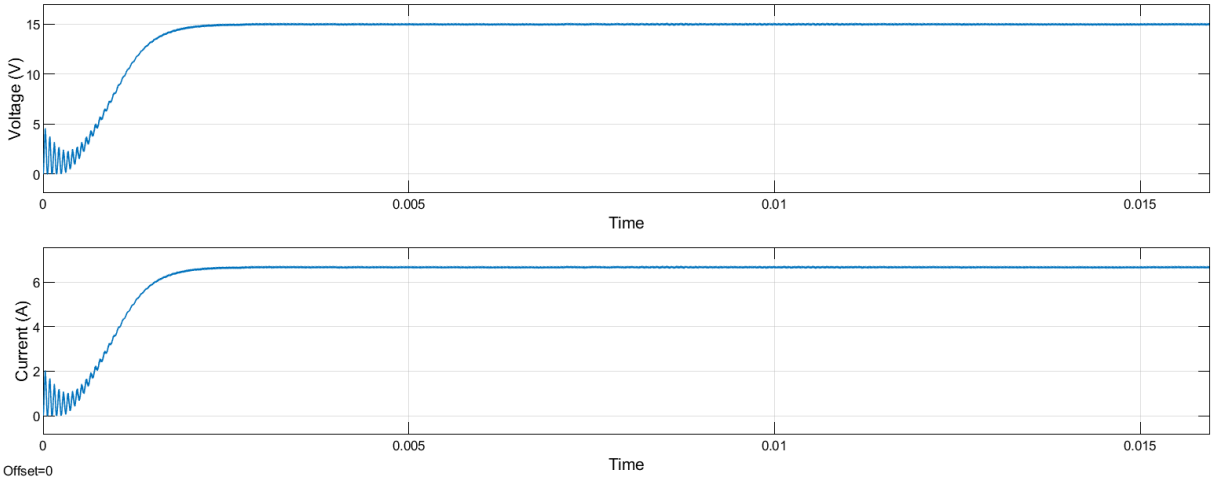

Figure 33- Voltage and current at the load.

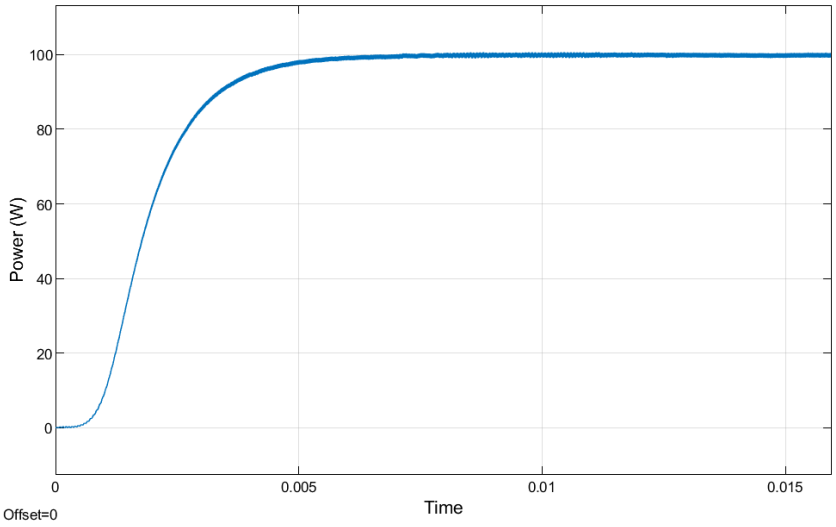

Figure 34- Power delivered to the load.

5. PCB design and manufacturing

After performing the simulation and analyzing the results derived from the software tests, this section focus on the PCB design that contains the primary and the secondary VSCs of the charger prototype. Both VSCS have the same full-bridge typology, which means their design is equal, with the only difference being that one's input is the other output since one converts DC to AC and the other AC to DC. Since MOSFETs are more adapted to high-frequency applications, both power converters were implemented using MOSFETs. A selection process is made from different models available at the market, evaluating their expected efficiency, cost, gate driving requirements, and packaging. This allowed finding the best candidate to be used on the primary and secondary converters.

After selecting the MOSFET, an overview of the design for the converters main elements was made. The schematics and drawings of all the PCBs made are included in appendix Appendix B- PCB Schematics.

5.1. Power Semiconductors

The two most popular transistor technologies for switched power converters are the MOSFET and the IGBT. When deciding which one to use, it is common to choose IGBT if the application has high-voltages and current ratings and low switching frequencies, but regarding low-voltage and currents with higher switching frequencies, the favorite is the MOSFET. Given the high frequencies that WCS's work, an obvious pick to integrate on the converter is the MOSFET since by being able to perform fast switching application, the turn-off losses are significantly lower than using an IGBT based converters..

5.1.1.Semiconductors Losses

MOSFET's losses can be divided into two categories:

- Conduction Losses - This loss relates to the RMS current that flows through the transistor channel.
- Switching Losses - This loss relates to the energy necessary to create and destroy the conductive channel that the transistor provides.

By adding both types of losses, conduction, and switching, it is possible to determine the total power dissipated by the MOSFET.

The conduction power losses consider the MOSFET's resistance when it is conducting, R_{DSon}. The instantaneous conduction power losses, P_{CON}, is expressed by the expression:

$$P_{CON} = R_{DSon} i(t)^2 \tag{42}$$

To obtain the average of the conduction power losses on the MOSFET, from the integration of equation (42) :

$$P_{CONavg} = \int_0^T R_{DSon} i(t)^2 = R_{DSon} I^2{}_{Srms} \tag{43}$$

Where the RMS current that goes throw the transistor while this is turn on is I_{Srms}:

The switching losses, P_{SW}, are the power losses during the rise and fall transition when the MOSFET is turned on and off. These can be calculated using the following expression [29]:

$$P_{sw} = \frac{1}{2} V_{dd} I_d (t_r + t_f) f_{sw} \tag{44}$$

From equation (43) and (44), it is possible to obtain the total dissipated energy by the MOSFET:

$$P_D = P_{CONavg} + P_{sw} \tag{45}$$

5.1.2.Thermal Model

Evaluating the thermal characteristics of the semiconductors selected for any application is an important limitation worth considering. To perform this thermal evaluation, designing a thermal model of the devices becomes very useful when searching for a possible candidate to integrate on the converter design. This model takes into consideration the temperatures of the junction given by each manufacturer and provides a limit to whether the device can withstand the rise of temperature expected or not. There is evidence that a MOSFET's lifetime depends highly on the average temperature and the temperature fluctuations in its junctions [33].

The temperatures that each device can withstand tend to vary from manufacturers as well from the package used. Since there are special packages that come with thermal enhancement. Besides packages, there is also a possibility of using a heatsink. The heatsink is responsible for cooling the semiconductors by connecting the device physically to the heatsink, as illustrated in Figure 35.

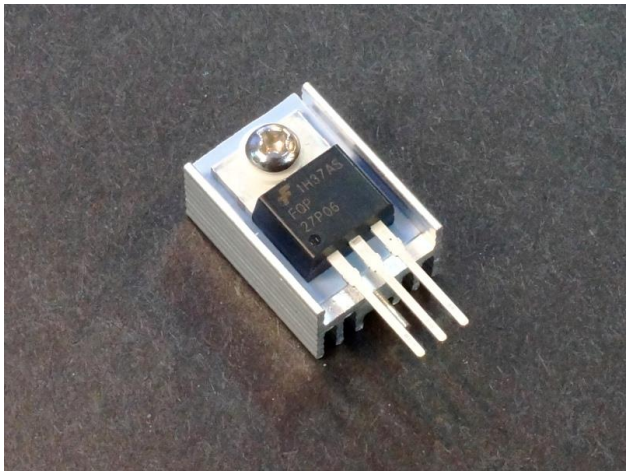

Figure 35- Example of a heatsink connected to a MOSFET

The model can be designed with a simplified steady-state analysis where it is assumed that temperature differences are propagated instantly or a transient analysis where the materials' thermal capacity is also taken into consideration. Since thermal models are not a point of interest in this thesis, only a steady analysis is made.

This thermic model takes into account the temperatures of the junction, T_j , of the MOSFET his case temperature, T_c , the ambient temperature, T_a, and if used the heatsink temperature, T_s. The temperature values between each part of the component are the thermal resistance that is given by the manufacturer, which consists of thermal resistance from junction to case, $R_{\theta j-c}$, from case to the heatsink, $R_{\theta c-s}$, and from the heatsink to the ambient, $R_{\theta s-c}$ measured in $℃/W$. As an analogy to the Ohm law, one can compare the heat flux to currents on an electric circuit, the temperature differences to voltages, and the thermal resistances serve the same as the electric resistances, as is shown in Figure 36.

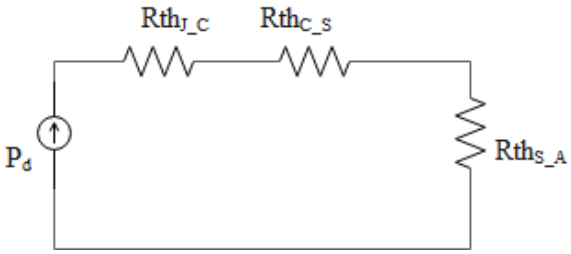

Figure 36- Equivalent circuit for the thermal model.

By analogy to ohm law, the following expressions can be written:

$$T_j = T_a + P_D(R_{\theta j-c} + R_{\theta c-s} + R_{\theta s-a}) \quad (46)$$

$$R_{\theta s-a} = \frac{T_j - T_a}{P_D} - R_{\theta c-s} - R_{\theta j-c} \quad (47)$$

When selecting a heatsink, the value of the thermal resistance between the heatsink and the ambient, equation(47), is essential to select the heatsink.

5.1.3.Semiconductor Selection

The MOSFETs selection process considers firstly the value of the voltage and current that goes through each semiconductor, then a way of evaluating a semiconductor is by performing a FOM analysis or "Figure of Merit." It is a handy tool because it considers both the conductions losses and the switching losses. It is calculated based on the drain to source On-resistance (RDSon) times the gate charge (Qg). The gate charge is the charge the gate of the MOSFET needs to turn on. It is relevant to mention that the FOM is not a physical feature of the MOSFET. It serves only as a reference to help select a semiconductor for this application. After performing the FOM analysis and selecting the most efficient model, the final step is to look at the thermal resistance given by its manufacturer. This parameter is essential because the MOSFET must have a thermal resistance high enough to tolerate the power dissipated during the switching process. MOSFET's with TO-220 packages are an excellent choice to start selecting from since they come with a physical feature that provides the possibility of adding a heatsink if the power dissipated becomes too high for the transistor to tolerate.

Three different models were selected to which two of which were from Infineon™ and one model from Fairchild-On Semiconductor™. All models have a TO-220 Full-Pak, which enables the connection between the MOSFET case junction to a heatsink.

Since the expected voltage across the DC link is around 15 V, it is unnecessary to use semiconductors with high breakdown voltage, which results in lower-priced semiconductors.

Table 6-Most relevant parameters of the selected MOSFETS.

Model	R_{DSon} [mΩ]	Q_g [nC]	FOM [n]	$R_{\theta j-c}$ [℃/W]	$R_{\theta j-a}$ [℃/W]	t_r [ns]	t_f [ns]	P_{Con} [W]	P_{sw} [W]	P_d [W]
FQP44N10	39	48	1.87	1.03	62.5	190	100	3.05	2.4	5.45
IRFI4410ZPbF	7.9	81	0.640	3.20	65	27	30	0.62	0.47	1.09
IPP180N10N3G	18	19	0.342	2.1	62	12	5	1.41	0.14	1.55

Table 6 lists the most relevant parameters of the three selected MOSFETS. Besides looking at each candidate's FOM, it is also essential to understand their capability of windstanding high temperatures resulting from the dissipated power from the conduction and switching losses.

A thermic model can be used to find the value of thermal resistance between the heatsink used and the environment surrounding the semiconductor. According to (47), assuming a value of thermal resistance between the case and the heatsink around the 0,05 ℃/W as well as a maximum junction temperature of 175℃, T_j, and an ambient temperature of 25℃, T_a, it is possible to obtain the thermal resistance between the heatsink and the ambient.

$$R_{\theta s-a} = \frac{1}{4}\left(\frac{T_j - T_a}{P_D} - R_{\theta c-s} - R_{\theta j-c}\right) \quad (48)$$

Since all the MOSFETs, 4 in total, used in each converter are glued to one standard heatsink and the value obtained for the thermal resistance between the heatsink and the ambient for each MOSFET, the total value of the thermal resistance between the heatsink and the ambient must be divided by 4.

Table 7-Parameters of the MOSFETS with the heatsink thermal resistance

Model	$R_{\theta j-c}$ [℃/W]	$R_{\theta j-a}$ [℃/W]	P_d [W]	$R_{\theta s-a}$ [℃/W]
FQP44N 10	1.03	62.5	5.45	6.61
IRFI4410 ZPbF	3.20	65	1.09	33.6
IPP180N 10N3G	2.1	62	1.55	27.7

The heatsink thermal resistance value must be lower or equal to the values obtained in Table 7 for each MOSFET selected.

By looking at table 1 and 2, the best option for this specific application is the model "IRFI4410ZZPbF" from Infineon™ [34] since it shows the least losses and has a relatively small thermic resistance,$R_{\theta j-c}$.

5.1.4.Gate Driver Design

The gate driver was designed according to instructions presented in the datasheet of the model "1ED020I12-F2" [35] from Infineon™. Each MOSFET has a gate driver responsible for supplying a signal turning on and off the semiconductor. This IC provides galvanic isolation between the controller circuit and the power circuit.

To avoid short circuits that might occur during the converter switching, the IC has a desaturation circuit that can detect if a short circuit was detected and turn off the semiconductor to avoid any possible damage. According to the manufacturer [35], the gate driver monitors the MOSFET drain-source (V_{DS}) to

detect desaturation caused by the short circuit. If the driver's output is high V_{DS} is above a defined value, and a specific blanking time has expired, the IC acts and switches off the MOSFET.

The passive components connected to the gate drive's output need to be sized for the specific values of current and voltage applied to the MOSFET selected.

The gate driver resistors at each IC are essential to control the speed of each transistor is trigged.. To size this resistance, an RLC was considered. R_g being the gate resistance, L_{pa} the parasitic inductance of the path to the gate of the device, including the physical connecting between the transistor and the PCB where it was mounted, and the input capacitance C_s. The gate resistance was selected considering a damping ratio of $\frac{1}{\sqrt{2}}$ proving a faster response:

$$R_g = 2\varepsilon Z_0 = 2\varepsilon\sqrt{\frac{L_{pa}}{C_s}} \tag{49}$$

The input capacitance can be calculated using the manufacturer capacitance parameters and the relation between the drain to source and gate to source voltage:

$$C_s = C_{iss} + C_{rss}\frac{V_{DS}}{V_{GS}} = 5nF \tag{50}$$

Assuming a width of $1.57\,mm$ of the PCB, the parasitic inductance is estimated to be around $23.07\,nH$ reaching the value:

$$R_g = 2\varepsilon Z_0 = 2\varepsilon\sqrt{\frac{L_{pa}}{C_s}} = 3.0\Omega \tag{51}$$

The short circuit protection is achieved according to the desaturation circuit provided by the manufacturer [35] of the gate driver. The circuit is illustrated in Figure 37:

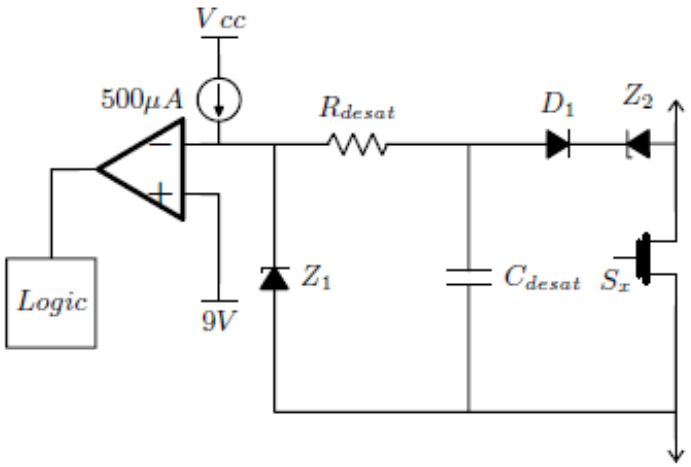

Figure 37-Short circuit protection circuit (Courtesy of Pedro Costa et al.).

The IC provides the $500\mu A$ precision current when the voltage at the capacitor C_{desat} exceeds the reference voltage of $9V$. This capacitor can be sized in the following way:

$$C_{desat} = \frac{I_{desat} t_{desat}}{V_{ref}} \tag{52}$$

The I_{desat} is the current of the current source, V_{ref} is the reference voltage of $9V$ and t_{desat} is related to the maximum short circuit time in the following way :

$$t_{sc} < t_{desat} \tag{53}$$

Where t_{sc} is the short circuit withstand the time of the transistor. According to the datasheet of the MOSFET selected "IRFI4410ZPbf" [34],a relatively good short circuit time that gives the maximum safe operating area is around 3 ms obtaining the value of the capacitor C_{desat} :

$$C_{desat} = \frac{I_{desat} t_{desat}}{V_{ref}} \approx 0.116\mu F \tag{54}$$

The Zener diode Z1 is used to protect the input pin. The Zener diode Z2 complements the drain to source voltage so that the reference voltage can be achieved in a short circuit. The short circuit time's value assumed that the drain to source voltage is around $5V$, making the Zener diode Z2 selected to have a forward voltage of $5.1V$.

5.2. Voltage and Current Sensing

The current measurement is done using a current transducer from BROADCOM," ACHS-7123" [36], which can measure current both in DC and AC. It has galvanic isolation between the control and power circuits. The IC uses a closed-loop hall effect technique for the measurement of the current. The current passing through the primary coil is estimated from the secondary current originated from the hall effect sensor. This transducer comes with many advantages such as excellent accuracy, excellent linearity, low-temperature drift, optimized response time, wide frequency bandwidth, no insertion losses, and high immunity to external interference and current overload capability. This model allows measuring current on a range of $\pm 36A$. The schematic of the current sensor is illustrated in Figure 38.

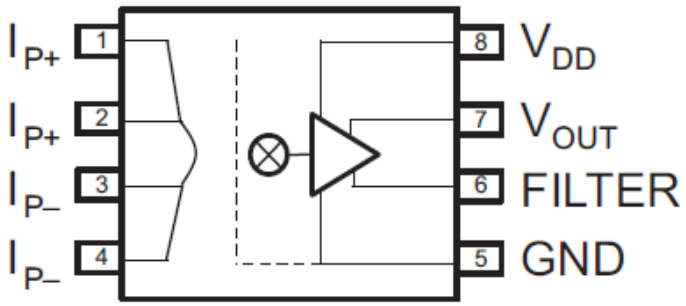

Figure 38- Current sensor schematic (Courtesy of BROADCOM LIMITED [36]).

Unlike the current measurement, in which its output signal is directly connected to the microcontroller, the voltage measurement is achieved by first using a voltage divider converting the high voltage supply from 0 to $15V$ to a lower range of 0 to $12V$. After the voltage divider, the signal is fed to a reinforced isolated amplifier, ISO224 [36] from Texas Instruments, so that it can be modulated by a delta-sigma modulator and then demodulated to a differential analog output of $\pm 4V$. This isolated amplifier comes with an isolation barrier between control and power circuit with high immunity to magnetic interference, providing galvanic isolation of up to $5kV$. It is necessary to use an operational amplifier so that the differential signal coming from the isolated amplifier can be converted to a single-end signal so that the ADC of the microcontroller can read the voltage measurements. The operational amplifier used is incorporated in the

IC of “ADA4177-2” [37] from Analog Devices that features a dual-channel amplifier with low offset voltage and drift, low input bias current, low noise, and low current consumption. The voltage sensing circuit described is placed on the primary converter's input and the secondary converter’s output. Figure 39 shows a schematic of the voltage sensing circuit.

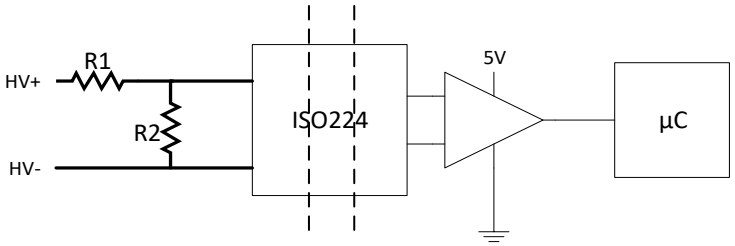

Figure 39- Voltage sensing schematic.

5.3. PCB Design

The PCB was designed using the open-source software KiCad EDA Suite [38]. KiCad is used for electronic schematic drawings and the creation of a printed circuit board. After specifically selecting each component, the next phase is the layout. In this layout phase, it is necessary to consider essential details. Many of the components selected, such as the MOSFETs, the voltage and current sensor, and the gate driver, need additional passive elements connected to them.

One of the most important factors to consider when designing a PCB is handling the maximum values of voltage and current expected during the charging process. First, to guarantee that the current isn’t going to damage the board, ensuring that the trace width selected for the power connection is thick enough is crucial, and then the low voltage signals should also be well suited for the maximum current expected. KiCad comes with a feature that makes it possible to calculate the recommended trace width given the expected current and the desired temperature rise using the standard IPC 2221 [39] :

$$I = K \times dT^{0.44} \times (W \times H)^{0.725} \tag{55}$$

Where I is the maximum current in amps, dT is the temperature rise above ambient in $deg\,C^{o}$, W, H are the width and thickness in mm, and K is a constant for if the tracks are internal or external. Since the RMS current coming from the DC link is around $7.5\,A$ and setting a temperature rise of no more than $50\ deg\,C^{o}$ o the trace width recommended is 0.9 mm, and so, the traces width were set to $1.5\ mm$, while the low voltage signal was set to $0.250\ \mathrm{mm}$ since the current is very low for control signals. The PCB has 2 layers in total, a width of $90.13\ mm$ and a height of $78.45\ mm$. The outer layer copper foil is $35\ \mu m$, which is enough to sustain the currents at the board for the trace width selected previously.

On the layout of the components, two relevant details are worth being mention. The first is that the heatsink was placed alongside the MOSFETs in a way that would be possible to connect them physically to the heatsink through the feature that the selected MOSFET comes. Finally, some special attention was given to the gate driver circuitry layout because the signal that commands the gate of each MOSFET of the converter must have the minimum inductance possible. All the gate drivers were placed near their respective semiconductor to ensure a driving signal's low inductance path.

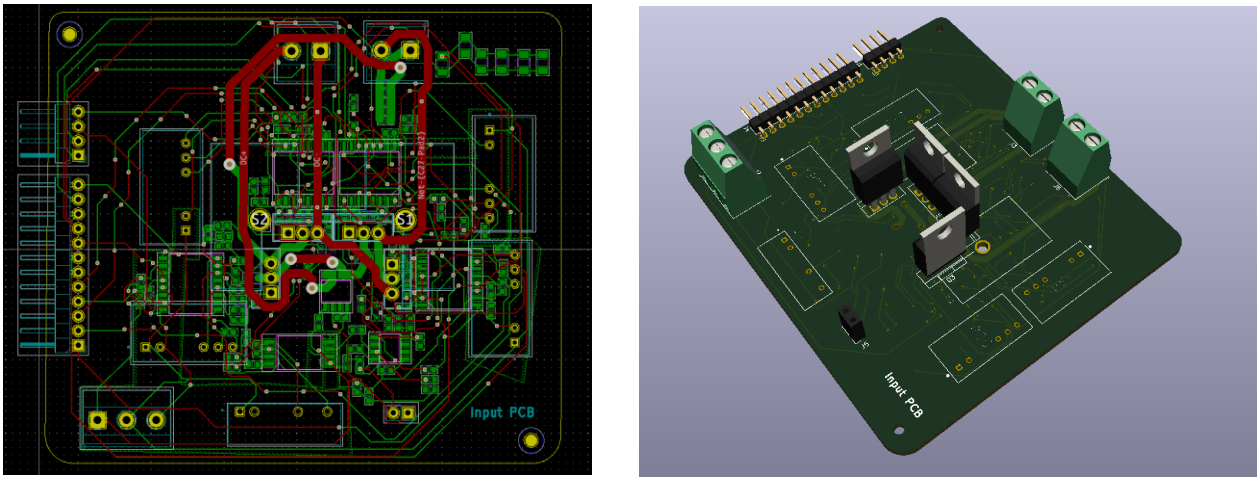

a) 2D view b) 3D view

Figure 40- KiCad PCB files

In Figure 40, both 2D and 3D files of the PCB can be observed. All the layout of the components selected were made to produce the most compact solution possible. Small changes on trace paths and components placement might make a more compact solution, but the obtained solution is good enough for what it is intended.

5.4. PCB Assembling

The PCB was ordered on Eurocircuits™. Eurocircuits is a company based in Belgium that specialized in manufacturing and assembling prototype and small series PCB's. After finishing all the PCB design, all the details containing the board's physical dimensions and features were sent to Eurocircuits™, which dispatched two printed boards, one to be used on the primary side and the other on the secondary side of the transformer. A picture of one of the printed PCBs from the bottom and top view before the rest of the components were soldered into the board is shown in Figure 41.

a) Top view b) Bottom view

Figure 41- PCB's before electric components were weld.

The components such as the MOSFETS, connecters, and heatsinks were placed on one side of the board, the top layer according to the configuration on KiCad, and the rest of the components were on the other side. This was done with the intention that all the components with a relevant height were placed on the same side of the board to avoid any complications when performing the experiments.

The SMD components were the first elements to be soldered in the board, and after that, the connectors were soldered. In this way, it was possible to test for any possible error regarding the low voltage systems' supply and correct it before soldering the MOSFETs and performing the charging tests. After the low voltage systems were tested, the high voltage circuitry composed of the MOSFETs and the heatsink was soldered on the board and then tested for any possible error. The complete assembly of both boards can be seen in Figure 42.

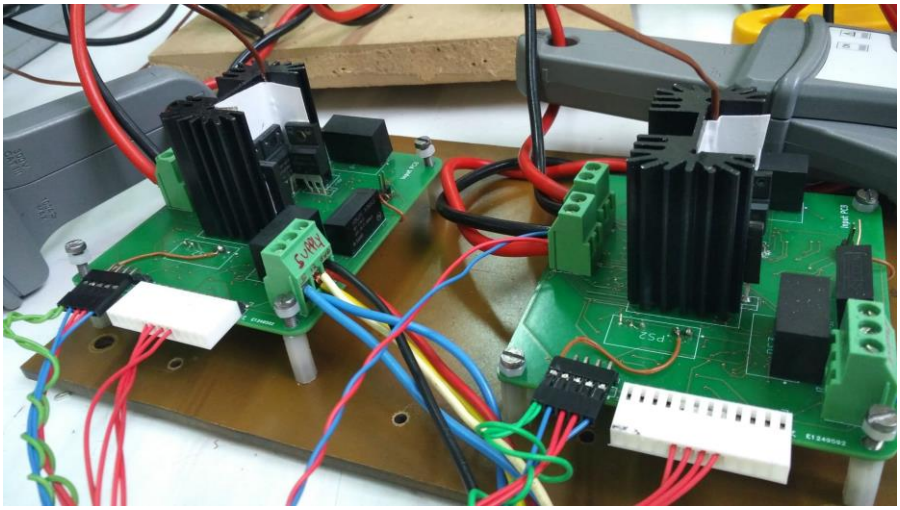

Figure 42-Total assembly

Some minor modifications were manually made on the board, given a couple of errors made when designing the PCBs regarding the gate drivers' control signals and the capacitors in the DC input entrance. These errors were later corrected, and the PCB schematics were updated.

6. Experimental Results

In this chapter, all the results from the experimental tests of the charger prototype are shown.

To test the converters, a PWM generator was programmed using a microcontroller. The microcontroller used was the model dsPIC33EV256GMM106 [40] placed on an evaluation board from Microchip [41]. For this specific application, a square wave is generated, switching between a voltage (on) and zero (off). By changing the portion of time that the signal spends on and off, usually designated by duty-cycle, which was set to 50 % of the wave period.

The phases between each PWM module, which this microcontroller has 3, is controllable by the user [40].In this way, it was possible to implement a phase-shift control similarly to the PI controller designed in chapter 3. The waveforms of the PWM signals generated by the microcontroller can be seen in Figure 43.

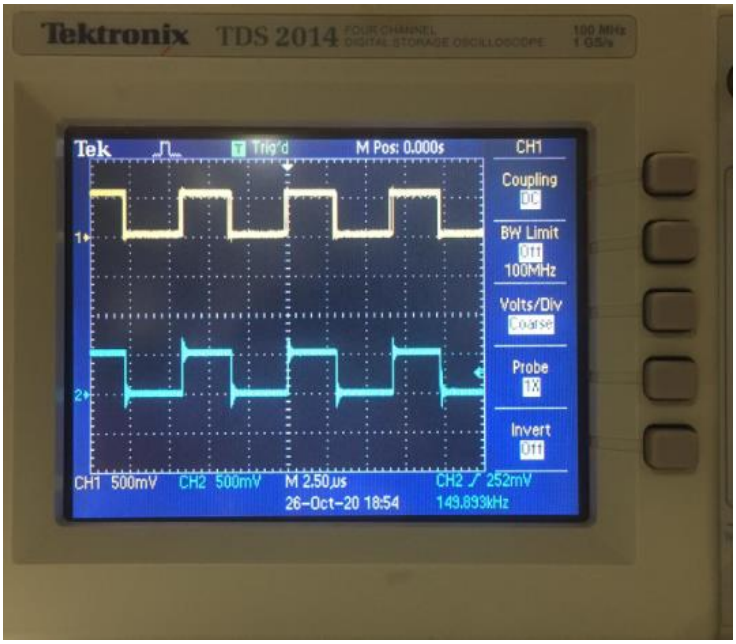

Figure 43-PWM signals-PWM1H (Yellow); PWM2H (Blue).

The microcontroller's PWM signals can be easily modified from a different range of frequencies available by the microcontroller [40]. Figure 43 illustrates the PWM signal with a frequency of $150\ kHz$ .The yellow square wave is the PWM1H and the blue square wave is the PWM2H. Since it is used a single-phase full-bridge topology for both converters, four signals are necessary to trigger the converter's arms. PWM1H and PWM1L for the converter on the primary and PWM2H and PWM2L for the converter on the secondary side. Also, to avoid triggering two MOSFETs of the same arm, a dead-time was set between each high and low signal.

Before assembling the final setup, preliminary tests were performed to ensure that the PWM generator's signals trigger the MOSFETs so that the converters on both boards work according to what is expected. The test was performed on both boards. A DC power supply was connected to the board's DC input, and a resistive load placed on the output. Two measurements were made: one was the PWM signals responsible for triggering one arm of the converter and the load current, illustrated in Figure 44. The results were the same for both boards, ensuring that the converters are working correctly.

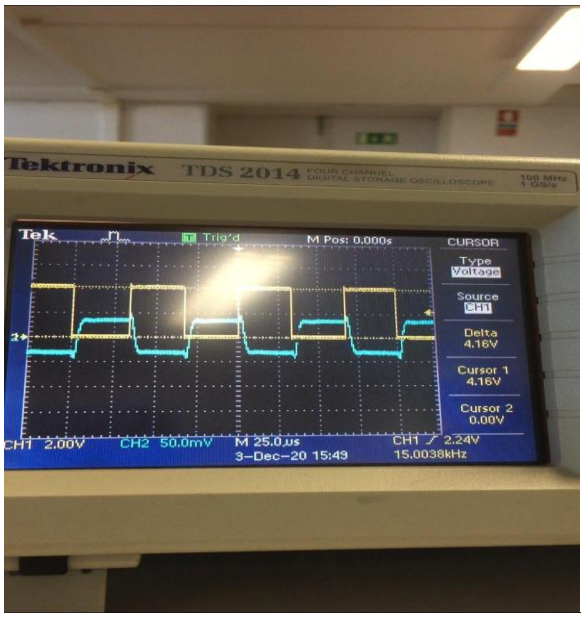

a) PWM signal (Yellow); Load Current (Blue).

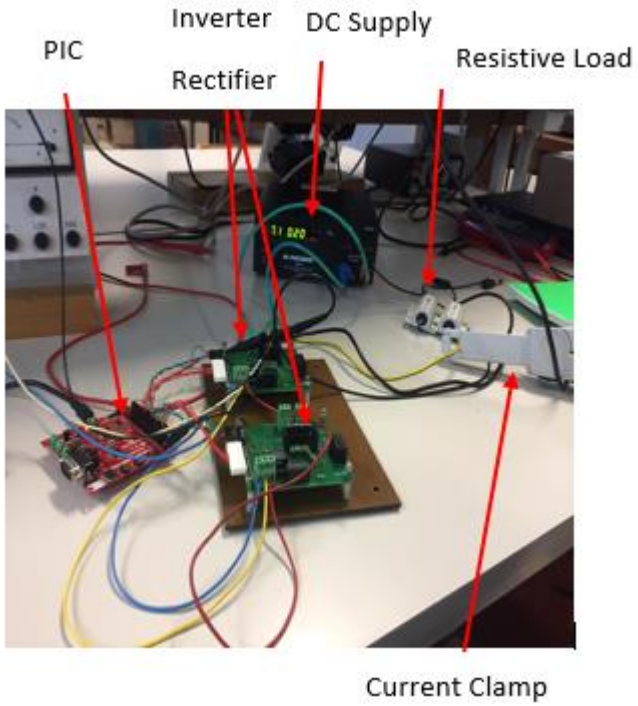

b) Test setup

Figure 44- Measurements and test setup.

Before selecting the switching frequency, it is essential to measure the resonant tank's wireless coils' self and mutual inductance. Having this new measurement helped in deciding which should be the switching frequency. Using an LCR Meter, the following values of self and mutual inductance of the wireless coils were measured:

Table 8- Measures of the wireless coils using an LCR instrument

Property	$L_p\,(\mu H)$	$L_s\,(\mu H)$	$M\,(\mu H)$
Value	7.11	6.8	3.95

The values in Table 8 were taken considering a gap between the primary and secondary coil of 5mm and that both coils were symmetrically aligned. These values are somehow different from the ones of the manufacture datasheet [28], since the magnetic circuits of each coil, namely the ferrite plates, influence

the other coil self-inductance. Figure 45 shows the wireless coil setup. An acrylic piece was used between the coils to fix the air gap height at 5 mm.

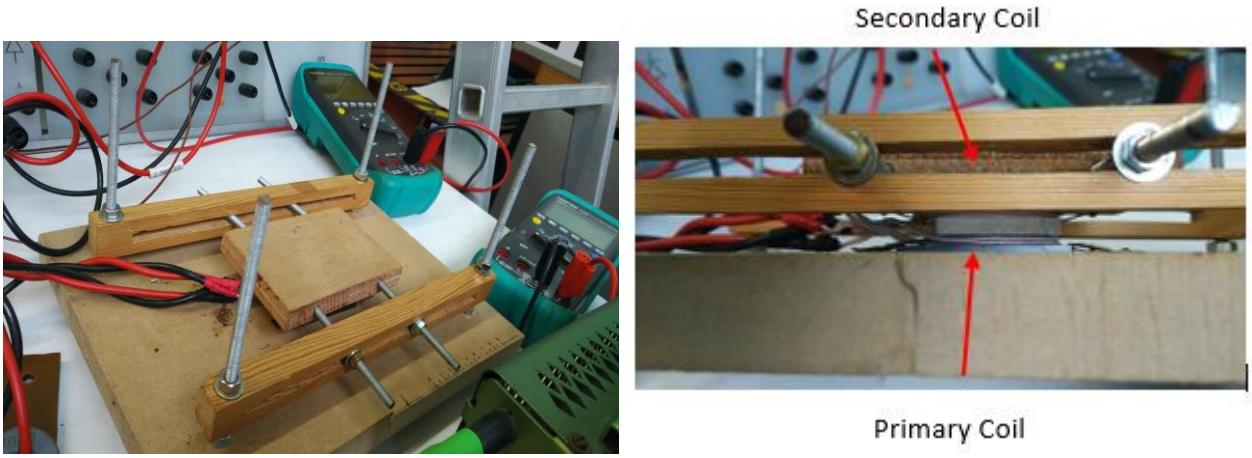

a) Wireless coils setup

b) Primary and secondary coils

Figure 45- Wireless coils setup.

The series capacitors of the resonant tank were added on both the primary and secondary boards to maintain the initial designated value of $0.47\ \mu F$. Using (8) again, the new resonant frequency can be obtained for both sides:

$$f_p = \frac{1}{2\pi\sqrt{L_p C_p}} = 87kHz \tag{56}$$

$$f_s = \frac{1}{2\pi\sqrt{L_s C_s}} = 88kHz \tag{57}$$

Both sides' frequencies are not equal because, even though similar, both coils have a different value of inductance, making the resonant frequency not precisely equal in both tanks.

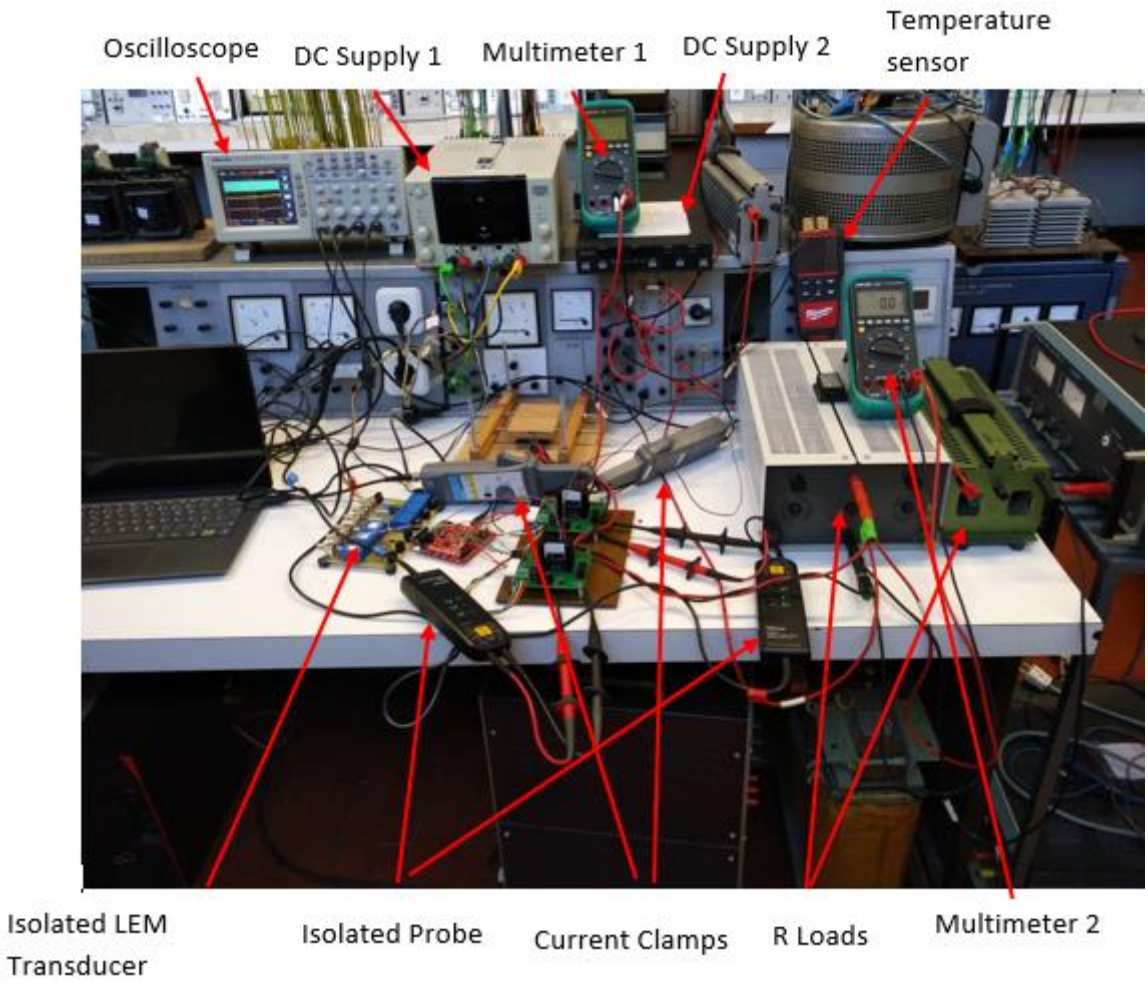

Figure 46- Full setup for the experiments.

The full setup of the experiment can be seen in Figure 46. This setup uses two DC supplies, one for the power transfer and the other to supply the low voltage to feed all the circuitry in both boards. A temperature sensor was connected to both heatsinks to ensure that temperature limits were not exceeded. There are two currents clamps, one in the input of the resonant tank and the other in the output, to obtain the current waveforms. At the output, two variable resistors were used, in this way, it is possible to adjust the load while doing the tests, and later they were used to test the controller's response to step on the load. A multimeter is used to measure the output voltage and the input voltage, and finally, to control the voltage, an isolated voltage transducer from LEM [41] was used to provide the DC voltage to the microcontroller the closed-loop control could be done.

To find the switching frequency that would lead to the best results, higher and lower frequencies relative to the resonant frequencies were set, tested, and analyzed individually regarding the relation between input and output power and quality of the current waveforms. As illustrated in Figure 47, the

frequencies with higher gain in power are between 85 and 98 kHz. The three phases in Figure 47 are the phase shift between the primary and secondary converter. As expected, the highest the phase shift produces the highest the output power, since demonstrated in equation (3), the active power is proportional to the phase shift between the primary voltage and secondary voltage of the resonant tank.

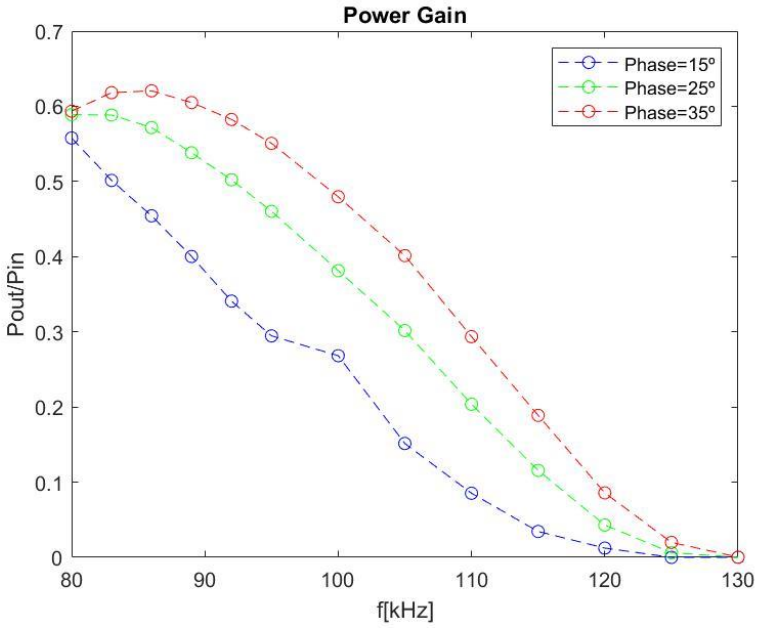

Figure 47- Power gain for three different phases

After testing for a set of frequencies between the ranges of 85 to 98 kHz, the frequency of 96 kHz seemed to be the one that produced better waveforms of current in the resonant tank combined with lower noise on the DC output, which is essential when applying the close control loop.

For the frequency of 96 kHz, to serve as another prove that higher phases produce higher output power values, Figure 48 shows the relation between the input and output power plotted against the phase shift between the command signals for the converters. The maximum value of power being delivered to the load is around 75 % of the power being supplied, ranging from the typical nominal efficiencies for wireless chargers [42].

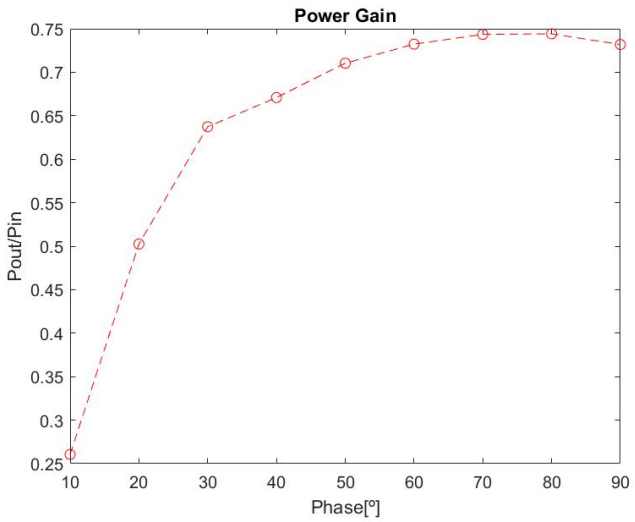

Figure 48-Power gain between phase shifts of 10º to 90 º

An example of the acquired data used to plot the graph in Figure 48 can be seen in Table 9. The frequency was fixed to 96 kHz, and then the phase shift between the primary and secondary was the only variable that was changed.

Table 9- Acquired data for 96 kHz and variable phase shift

$Phase[º]$	$V_{in}[V]$	$I_{in}[A]$	$V_{out}[V]$	$I_{out}[A]$	$P_{in}[W]$	$P_{out}[W]$
10	5	0.31	1.98	0.20	1.55	0.40
20	5.02	0.66	3.89	0.42	3.31	1.66
30	5.04	1.21	5.88	0.66	6.09	3.88
40	5.04	1.97	7.63	0.87	9.92	6.66
50	5.05	2.78	9.26	1.07	14.03	9.97
60	5.05	3.58	10.66	1.24	18.07	13.23
70	5	4.2	11.54	1.35	21	15.61
80	5.06	4.62	12.14	1.43	23.37	17.39
90	5.02	4.83	12.23	1.45	24.24	17.74

Before testing the closed-loop controller, the current and voltage waveforms in the resonant tank can be seen in both Figure 49-a) and Figure 49-b). In Figure 49-a), the voltages were measured at the DC stage of both the primary converter and secondary converter where the controller is phase-shifting the input voltage waveform of the secondary converter and the output voltage of the primary converter. In Figure 49-b), the voltage measurement at the load stage had some considerable noise, even though this the controller was able to maintain the voltage at the reference value.

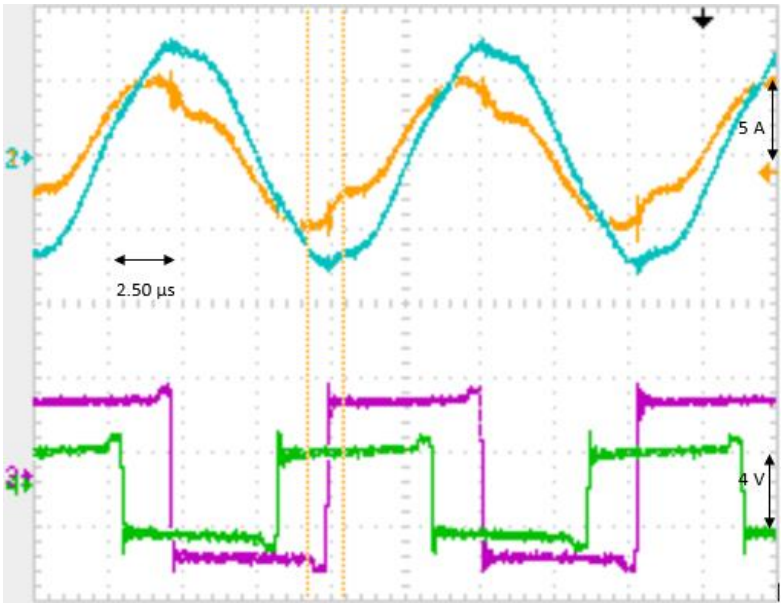

a)

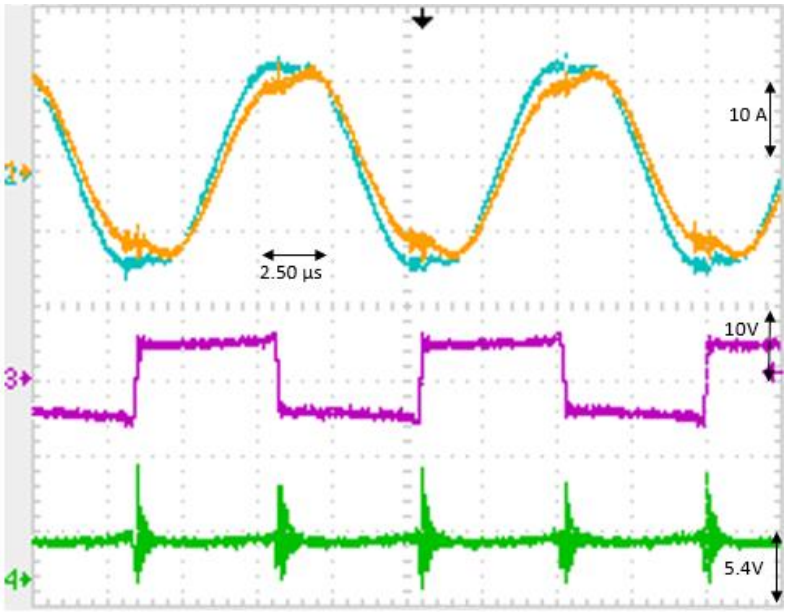

b)

Figure 49- a)-Input current of the secondary converter (orange), Output current of the resonant tank (blue), Input voltage of the secondary converter (purple), Output voltage of the primary converter (green);b)- Input current of the resonant tank (orange), Output current of the resonant tank (blue), Input voltage of the secondary converter (purple), Output voltage at load (green).

The controller was designed to track a reference output voltage. A load was connected in parallel with a manual switch to test the controller's response to an applied step in power. By turning on the switch, a resistive load is placed in parallel with the load stage, causing the output current to increase. The controller must adjust the phase shift between the primary converter and the secondary converter to maintain the load

voltage. Figure 50 and Figure 51 illustrate the controller's response to the increase of current when the switch is turned on and the decrease of current when the switch is turn off, respectively. Also, in Figure 52, it is possible to see both transients with an increase of the load current and a decrease of the load current. According to Figure 49, the controller takes proximally 2.50 ms to correct the voltage change at the load, which is considered acceptable since it is close to the controller's time response when designed and tested in the Simulink, as illustrated in Figure 32.

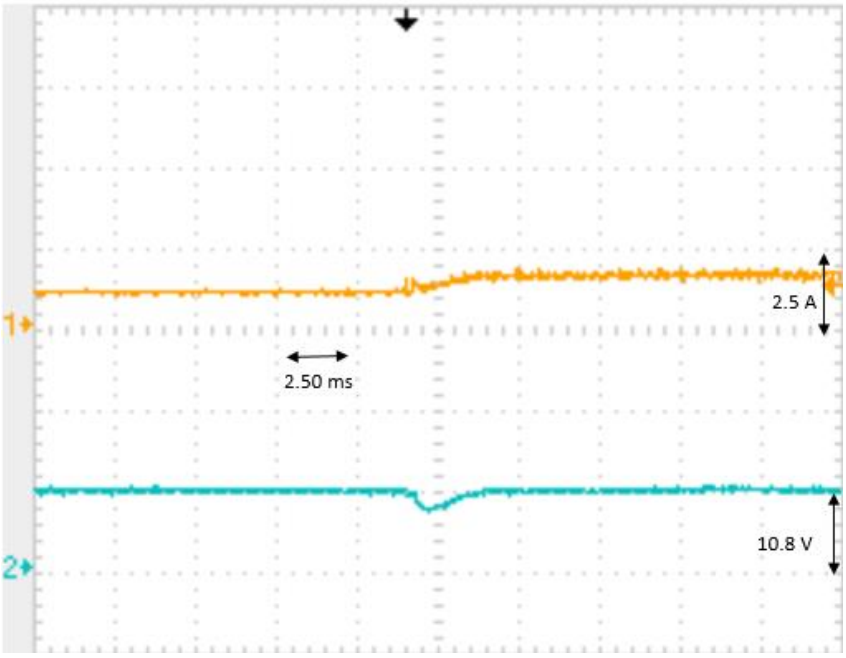

Figure 50- Turn on-Current (Orange); Voltage (Blue).

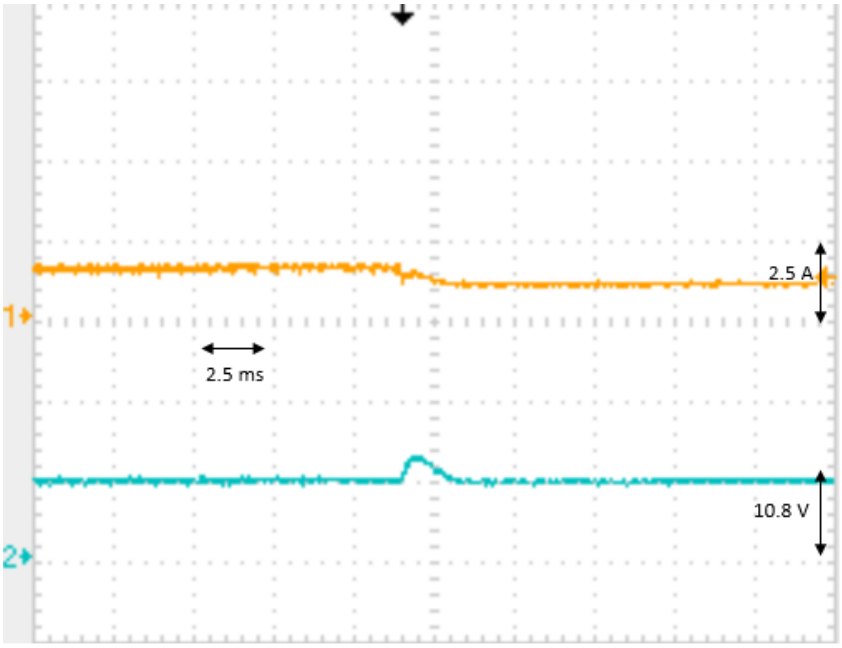

Figure 51-Turn off-Current (Orange); Voltage (Blue).

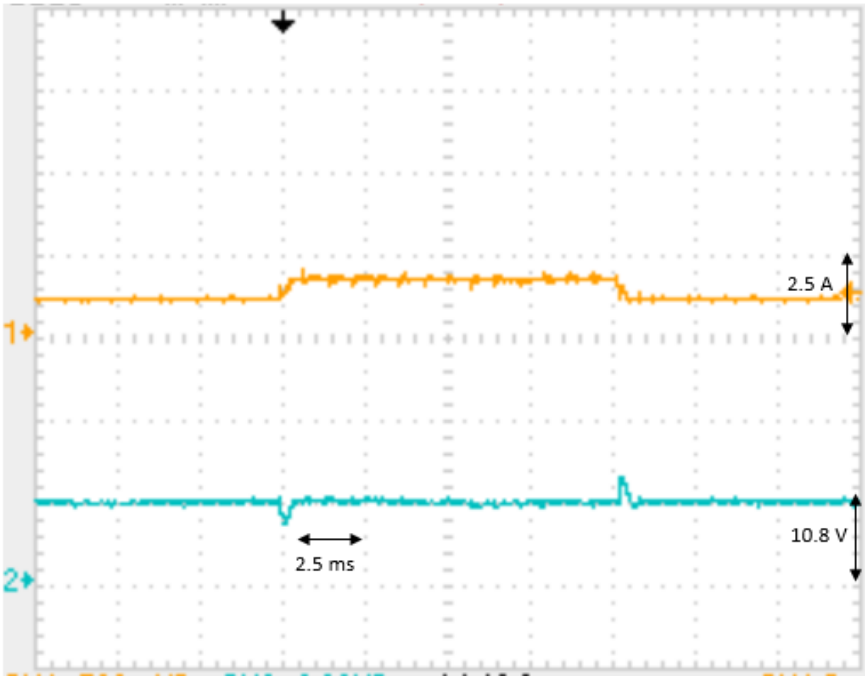

Figure 52-Turn on and off-Current (Orange); Voltage (Blue).

7. Conclusion

All the research done in this master thesis was aimed to understand better the process of designing and implementing a wireless inductive charger. After reviewing which current technology of wireless charging seemed, the more promising a prototype was developed.

The wireless charging prototype simulation was essential to understand the limitations of the converters' operational frequency and the overall efficiency of the charging process using the selected series-series compensation technology. The results obtained by the simulation were used as a base to decide which semiconductors technology to be used in the prototype. The phase-shift between the primary and secondary converter implemented by the PI controller showed a relatively simple way of guaranteeing a maximum transfer of power during the charging process.

With all the results gathered from the simulation, the PCB's design and manufacture were made. The PCBs had to be given minor adjustments due to some mistakes made during the design and the lack of time to correct the schematics and order a new version of both boards. Despite this, all the electric circuitry implemented in the board seemed to be working according to plan except the voltage sensor. The signal coming from the voltage sensor wasn't correct due to some error made during the sensor circuitry design, which caused the controller not to work correctly. To circumvent this, an additional isolated voltage sensor was added, which resolved the issue.

The experiments were limited to the equipment available at the Laboratório de Máquinas of Alameda Campus of Instituto Superior Técnico, which was enough given the relatively simple tests chosen to perform. The experiments of the prototype showed very high sensitivity to selected switching frequency, in a way that only a specific range of frequencies should be selected to guarantee the highest gain possible of energy transferred, serving as proof of the concept of wireless charging using a resonant tank to enable the power transfer.

7.1. Achievements

The main achievement obtained in this master thesis was the design and development of a prototype of a wireless charger. To truly understand the principles of how a wireless charger works, by building a prototype to simulate the wireless charging process, it was possible to analyze and understand the details that go through when planning and designing a real wireless charger.

The objectives achieved in this thesis were:

- The state-of-art of WPTS were reviewed, and one technology was selected to further investigated;

- Designed a prototype of a Wireless Charger using a Series-Series Compensation topology;
- The selected topology was analyzed in both simulation and experimental testing;
- A control system was designed to command the semiconductors;
- Design and build an experimental prototype to validate both the designed controller and the selected topology;
- Results of both analytical and experimental tests were included in the master thesis, along with the schematics and documentation regarding the prototype so that a platform is created for future improvement.

7.2.Future work

During the development of this master thesis, the primary goal of building and testing a wireless charger was always maintained even though some modifications had to be made regarding the number of experiments and simulations that was initially planned because mainly of time restraints and prolonged times of waiting for parts of both PCB circuitry that were essential to complete the experiments.

Regarding the simulations performed to test the inductive charger, besides controlling the voltage at the load, it would be beneficial also to control the current being supplied to the load in this way fully model of a battery could also be tested, becoming an even more realistic simulation of a wireless charger.

In what concerns the experimental measurements, it would also be interesting to analyze the charger's behavior when misalignments and changes of high between the coils are introduced since, in a realistic setting, this usually occurs.

Some results obtained from these experiments did not go through further investigation, such as noise in some of the measurements. This was overlooked due to the small power injected by the source, which didn’t produce a high enough ripple to impair the controller from working correctly, but if testing for higher power ratings, this is an eventual obstacle that should be further studied.

Finally, other possible experiments that should be done for further data collection are experimenting with other compensation topologies such as series-parallel, parallel-series, parallel-parallel, or other more sophisticated combinations to observe the behavior of the charger when switching topologies. The capacitors containing the resonant tank should be placed outside from the PCBs to be more convenient to alternate between topologies without needing to change the PCB’s layout completely.

References

[1] I.-I. E. Agency, "Global EV Outlook 2020," 2020. [Online]. Available: https://www.iea.org/reports/global-ev-outlook-2020.

[2] M. Woodward, D. B. Walton, D. J. Hamilton, G. Alberts, S. Fullerton-Smith, E. Day and J. Ringrow, "Electric vehicles-Setting a course for 2030," *Delloite Insights,* 2020.

[3] S. Abraham, K.Ganesh, A. SenthilKumar and Y. Ducqd, "Impact on Climate Change Due to Transportation Sector – Research Prospective," *Procedia Engineering Volume 38,* pp. 3869-3879, 2012.

[4] W. H. Organization, "Health and sustainable development.," 2014. [Online]. Available: https://www.who.int/sustainable-development/transport/health-risks/climate-impacts/en/.

[5] C. E. Regulator, "Market Snapshot: How much CO2 do electric vehicles, hybrids and gasoline vehicles emit?," 2020. [Online]. Available: https://www.cer-rec.gc.ca/en/data-analysis/energy-markets/market-snapshots/2018/market-snapshot-how-much-co2-do-electric-vehicles-hybrids-gasoline-vehicles-emit.html.

[6] A. K. Basu, S. Tatiya and S. Bhattacharya, "Overview of Electric Vehicles (EVs) and EV Sensors," in *Sensors for Automotive and Aerospace Applications*, 2019, pp. 107-122.

[7] C. Iclodean, B. Varga, N. Burnete, D. Cimerdean and B. Jurchiș, "Comparison of Different Battery Types for Electric Vehicles," *IOP Conference Series: Materials Science and Engineering 252 ,* pp. 1-10, 2017.

[8] A. M. Research, "Global Wireless EV Charging Market," 2020. [Online]. Available: https://www.alliedmarketresearch.com/wireless-electric-vehicle-charging-market.

[9] N.Tesla, "System of Transmission of Electrical Energy," *U.S. Patent 645,576,* 1900.

[10] C. Panchal, S. Stegen and J. Lu, "Review of static and dynamic wireless electric vehicle charging system," *Engineering Science and Technology,Volume 21,Issue 5,Elsevier,* pp. 922-937, 2018.

[11] O. Stielau and G. Covis, "Design of loosely coupled inductive power transfer systems," *Int.Conf. On Power System Technology, PowerCon., 2000, vol 1,* pp. 85-90, 2000.

[12] Z. Liu, H. Zhao, C. Shuai and S. Li, "Analysis and Equivalentof Four-coil and TwoCoil Systems in Wireless Power Transfer," *IEEE PELS Workshop on Emerging Technologies: Wireless Power,* pp. 1-5, 2015.

[13] Z. Bi, T. Kan, C. C. Mi, Y. Zhang, Z. Zhao and G. A. Keoleian, "Review of wireless power transfer for electric vehicles: Prospects to enhance sustainable mobilit," *Elsevier.Volume 17,* pp. 413-425, 2016.

[14] K.Aditya, V.Sood and S.Williamson., "Magnatic characterization of unsymmetrical coil pairs using archimedean spirals for winder misalignaments tolerance in IPT systems.," *IEEE Transactions on Transportation Electrification, VOL. 3, NO. 2,,* pp. 453-463, 2017.

[15] L. Weilai, "High efficiency wireless power transmission at low frequency using permanent magnet coupling," B.A.Sc, University of British Columbia, 2007, Vancouver, 2019.

[16] M. Fariborz and E. Wilson, "Overview of wireless power transfer technologies for electric vehicle battery charging," *IET Power Electronics, Volume: 7, Issue: 1,* pp. 60-66, 2014.

[17] J. Vázquez, P. Roncero-Sánchez and A. P. Torres, "Simulation Model of a 2-kW IPT Charger with Phase-Shift Control: Validation through the Tuning of the Coupling Factor," *Electronics 2018, 7, 255. Electronics 2018, 7, 385,* pp. 2-19, 2018.

[18] C.Wang, G.Covic and O.Stileau, "Design considerations for a contactless eletric vehicle battery charger," *IEEE Transactoins on Industrial Electronics. Volume: 52, Issue: 5,* pp. 1308-1314, 2005.

[19] J.Sallán, J.Villa and A. a. J.Sanz, "Optimal Design of ICPT Systems Applied to Electric Vehicle," *IEEE Trans. Ind. Electron.Volume:56,Issue:6,* pp. 2140-2149, 2009.

[20] Y. Sohn, E. Lee, G. Lim, G. Cho and C. Rim, "General Unified Analyses of Two-Capacitor Inductive Power Transfer Systems: Equivalence of Current-Source SS and SP Compensations," *IEEE TRANSACTIONS ON POWER ELECTRONICS, VOL. 30, NO. 11,* pp. 6030-6045, 2015.

[21] S.Li and C.Mi., "Wireless power transfer for eletric vehicle applications.," *IEEE Journal of Emerging and Selected Topics in Power Electronics,Volume: 3 , Issue: 1.,* pp. 4-17, 2015.

[22] A. T. Duarte M.Sousa, "Analysis of an inductive charging system for a commercial electric vehicle," - *Proceedings of the 2011 14th European Conference on Power Electronics and Applications, EPE 2011,* pp. 1-10, 2011.

[23] S. Subramaniyam and Lokeshwar, "Design of Single Phase High Frequency Inverter for Wireless Charging Application," *International Research Journal of Engineering and Technology (IRJET) Volume: 06 Issue: 05,* pp. 7568-7570, 2019.

[24] M. H. Rashid, S. Y. Hui and H. S.-H. Chung, "Resonant and Soft-Switching Converters," *Power Electronics Handbook (Fourth Edition),* pp. 339-382, 2018.

[25] K.-H. Liu and F. C. Lee., "Zero-voltage switching technique in DC/DC converters," *1986 17th Annual IEEE Power Electronics Specialists Conference,* pp. 58-70, 1986.

[26] N. Mohan, T. M.Undeland and W. P.Robbins, "Power Electronics: Converters, Applications, and Design," in *Power Electronics: Converters, Applications, and Design*, Toronto, Jonh Willey & Sons, INC., 1989, pp. 249-295.

[27] E. Wittenbreder, "Leakage Inductance (Part 1): Friend Or Foe?," HOW2POWER TODAY " Your Power Design Newslette", 2015.

[28] W. Elektronik, *Wireless Charging Coils WE-WPCC Transm Qi 5.8uH 18A 0.012Ohms.,* Revision 001.001, 2017.

[29] P. Costa and J. Silva, ""Compact Three-Phase SiC Inverter for the IST Formula"," 2018.

[30] M. Vujacic, M. Hammami, M. Srndovic and G. Grandi, "Theoretical and Experimental Investigation of Switching Ripple in the DC-Link Voltage of Single-Phase H-Bridge PWM Inverters," *Energies 2017,* pp. 1-16, August 2017.

[31] G. Ellis, Control System Design Guide:Using Your Computer to Understand and Diagnose Feedback Controllers, Elsevier Inc. 4th edition, 2012.

[32] M. Simulink, *Version 9.8.0(R2020a),* Natick, Massachusetts , 2020.

[33] Z. Sinan and B. Mutlu, "Lifetime Estimation of DCM Flyback Micro-inverter," *7th International Ege Energy Symposium & Exhibition,* pp. 1-10, 2014.

[34] Infineon Technologies, "IRFI4410ZPbF HEXFET® Power MOSFET," Rev 2017, 2015.

[35] Infineon Technologies, "1ED020I12-F2 - Single IGBT Driver IC," Rev. 2.1, 2017.

[36] BROADCOM Limited, "(Datasheet)ACHS-7121/7122/7123 Fully Integrated, Hall Effect-Based Linear Current Sensor IC with 3 kVRMS Isolation and Low-Resistance Current Conductor," 2018.

[37] Analog Devices Inc., "(Datasheet)OVP and EMI Protected, Precision,Low Noise and Bias Current Op Amps," 2018.

[38] Kicad, "KiCad Version(5.1.6)," 2020.

[39] Generic Standard on Printed Board Design . Standard, IPC, "Association Connecting Electronics Industries, Bannockburn, Illinois, 20," 2012.

[40] Mircochip, "(Datasheet)dsPIC33EV256GM106 - 5V Robust DSC with CAN, Safety, Motor Control,5," REV G., 2019.

[41] Mircochip, "(Datasheet)dsPIC33EV 5V CAN-LIN STARTER KIT, 11," REV A., 2014.

[42] E. Rubin, C. Kido, P. May-Ostendorp, C. Mercier and K. Dayem, "Global Forecast of Energy Use for Wireless Charging," Electronic Devices & Network Annex EDNA , July 2019 .

[43] Texas Instruments , "(Datasheet)ISO224 Reinforced Isolated Amplifier with Single-Ended Input of ±12 V and Differential Output of ±4 V," Revised 2018, 2018.

[44] P. Vinciarelli., "Forward Converter Switching at Zero Current," *U.S.Patent 4,416,959,* pp. 58-70, 1983.

[45] LEM, "Voltage Transducer LV 25-P," Version 19, 2014.

Appendix

Appendix A- Simulink Simulation

A.1 – Simulation block diagram

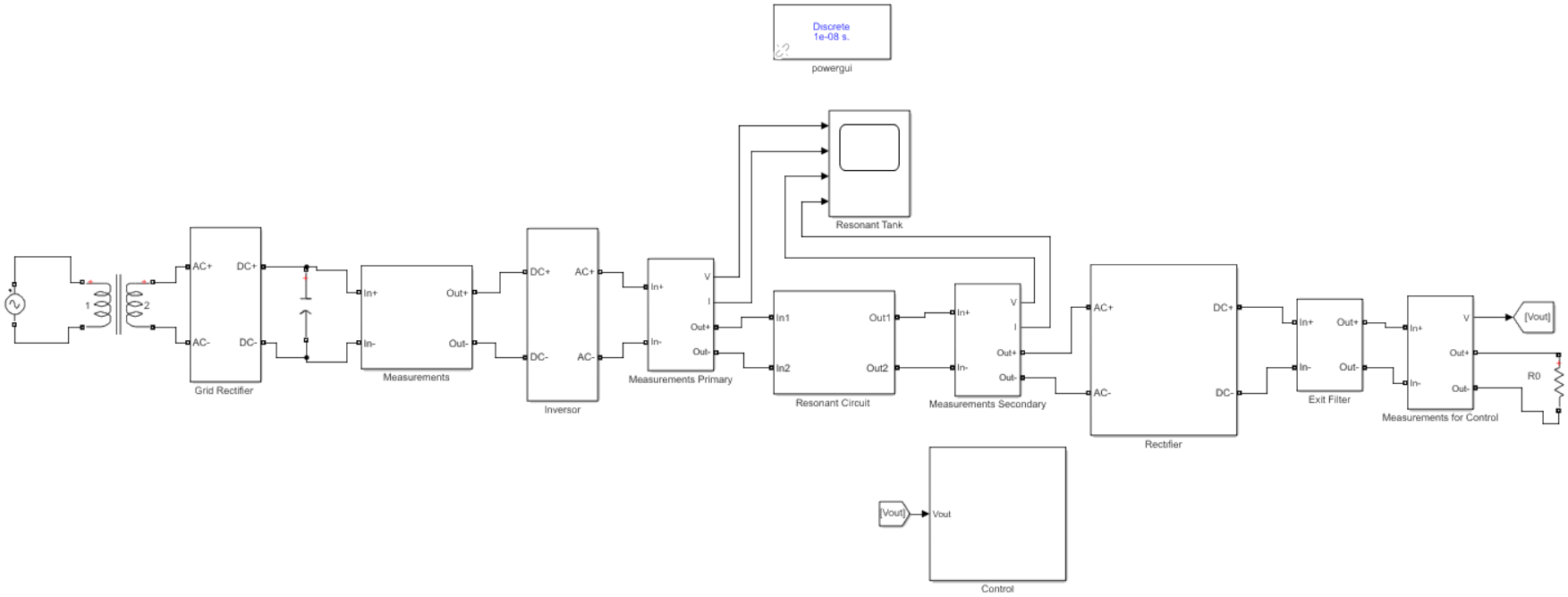

Appendix B- PCB Schematics

B.1 - Input Connections Schematic

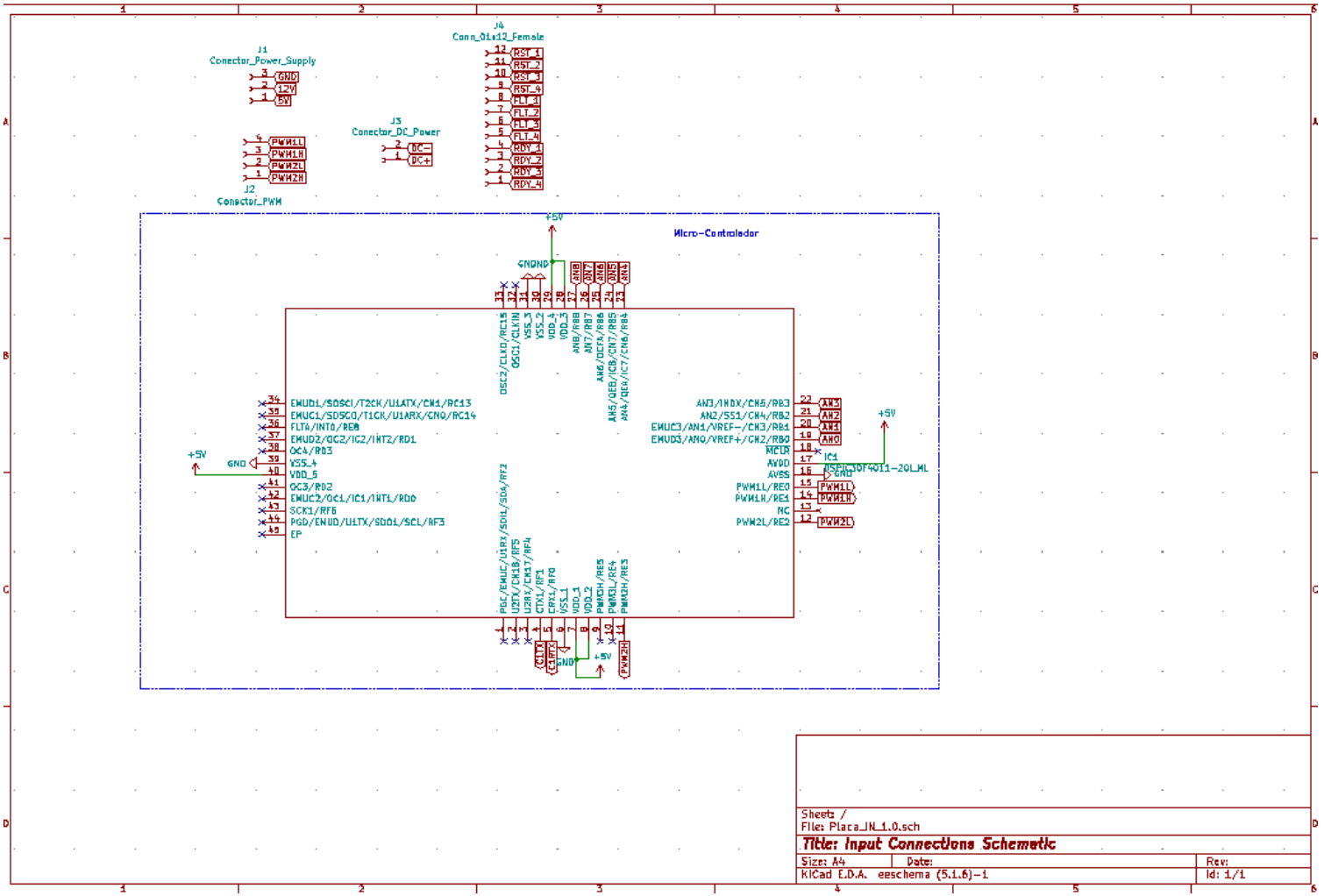

B.2 - Gate Driver Schematic

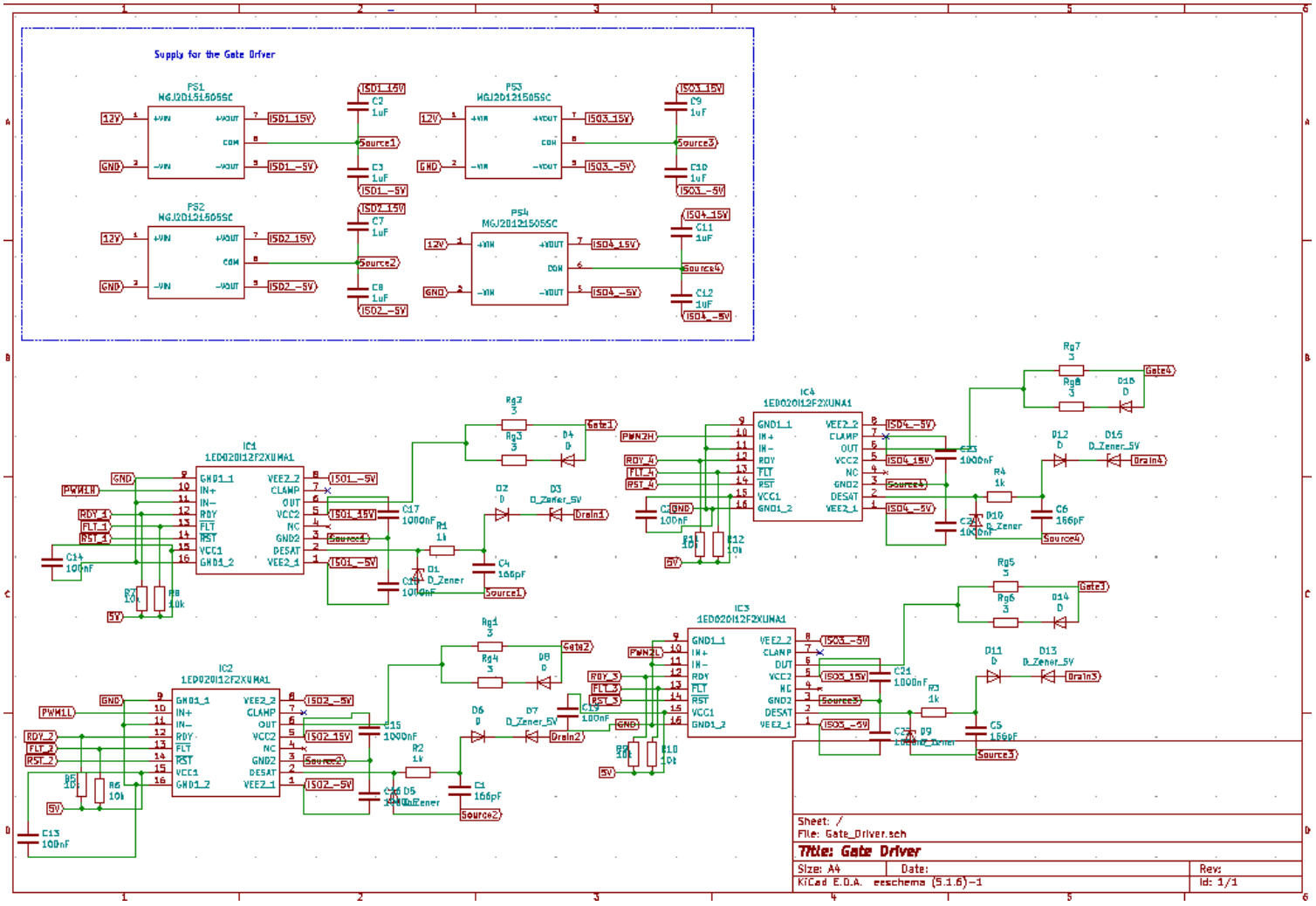

B.3 - Voltage and Current Sensor Schematic

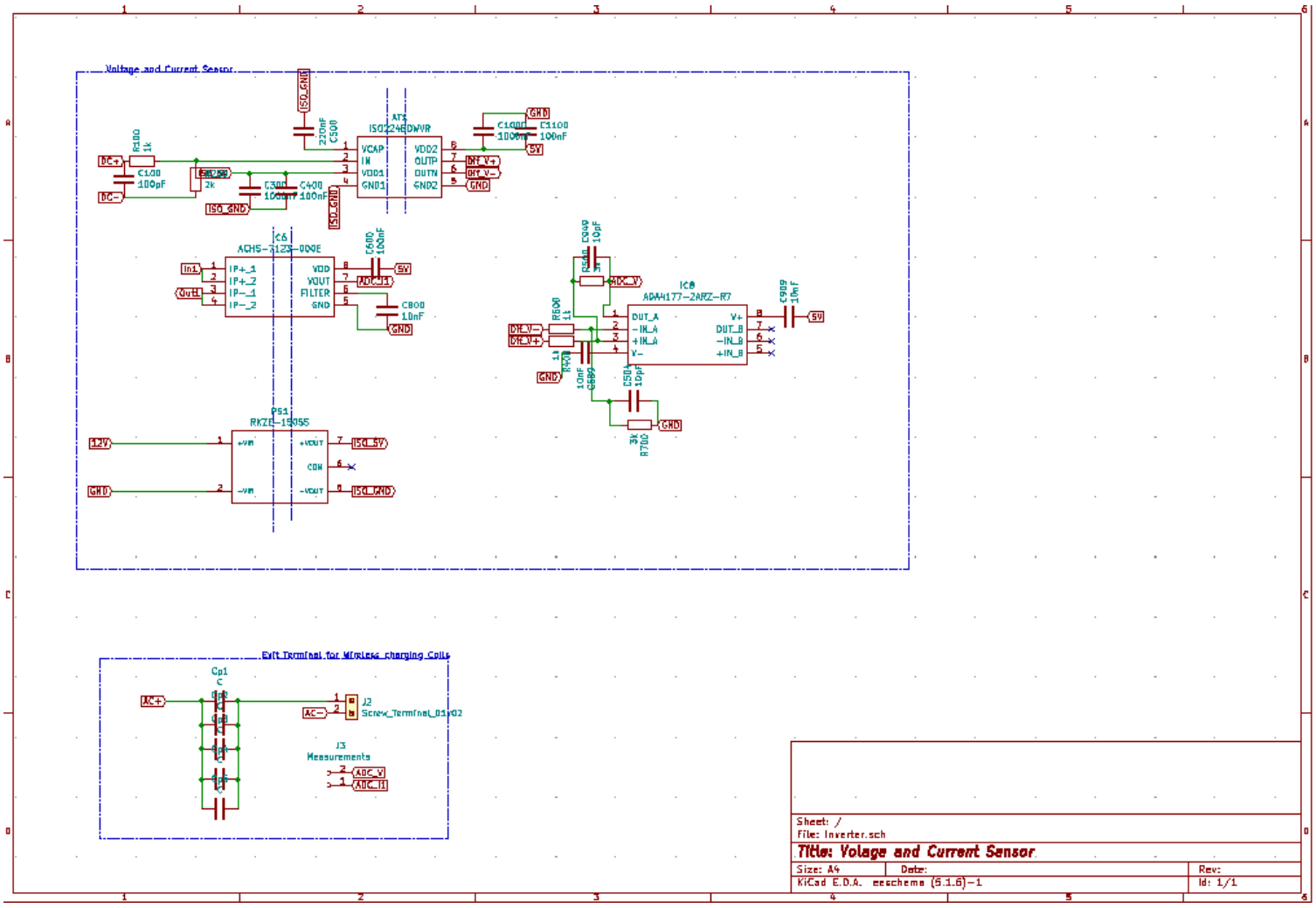

B.4 - Inverter Schematic

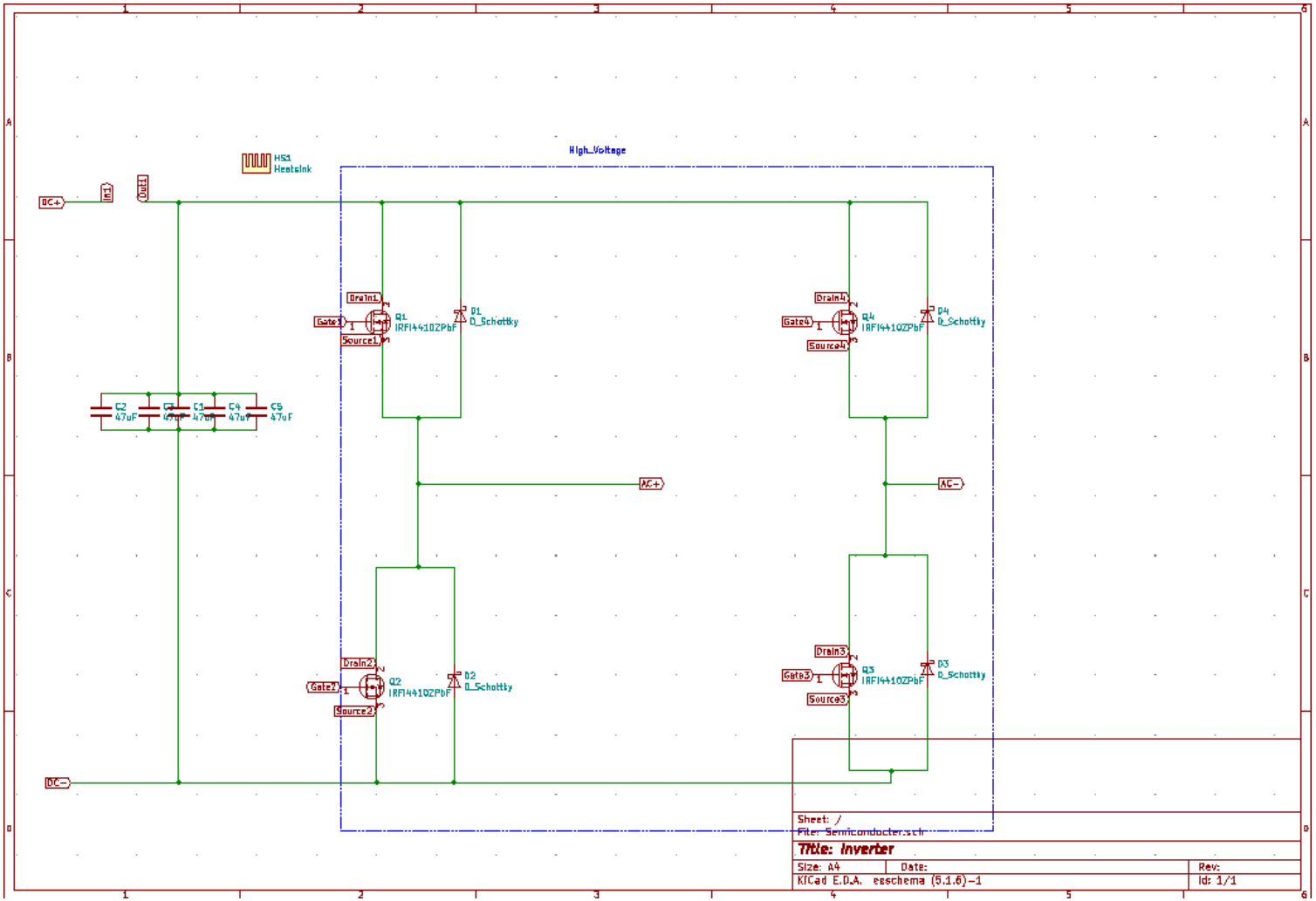

Appendix C- PCB Board Drawings

C.1- Top Layer

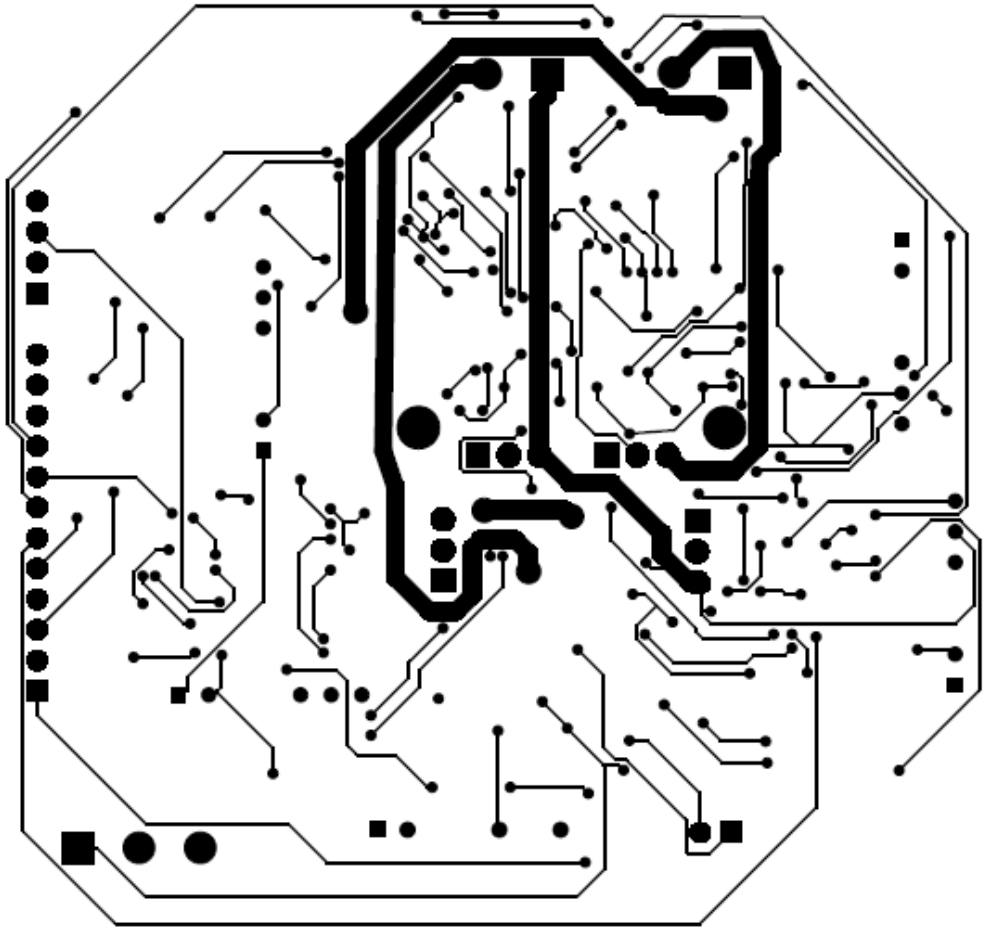

C.2- Bottom Layer